
4 Attitude System

Attitude determination is a requirement for most navigation and control problems. Classically, this problem has been solved by an Attitude Heading Reference System (AHRS) using gyroscopes that are updated by gravity sensors (pitch and roll) and magnetic field sensors (yaw) with low-pass filters to attenuate errors incurred during turns. Rate gyroscopes are prone to bias- and random-walk errors resulting from the integration of wide-band noise. Successful AHRS requires very expensive sensors that have exceptional bias stability. The sensor cost for this kind of attitude determination has limited such AHRS to very expensive applications. In cost-sensitive applications, filtering techniques are applied to bound the attitude error growth when using lessor sensors. With the recent

proliferation of low cost inertial sensors along with position and attitude sensors like the Global Positioning System (GPS), it has become viable to construct inexpensive attitude determination systems which have attitude errors that are bounded in time.

Recently, a considerable amount of effort has been directed at developing low cost systems for attitude determination. For example, [83] discusses an inexpensive attitude determination system for aviation applications. This attitude determination system does not employ any inertial sensors. Instead, it relies on a kinematic model of the vehicle along with GPS position and velocity measurements derived from a single GPS antenna to generate what is termed “pseudo-attitude.” A different approach is taken by [63], where a triad of inexpensive automotive-grade rate gyroscopes are fused with an ultra-short baseline GPS attitude determination system. In this system, the high bandwidth attitude information derived from integrating the output of the rate gyroscope was blended with the low bandwidth GPS attitude solution using a complementary filter. However, because the rate gyroscopes used possess poor bias stability, the GPS attitude system was used to continuously update the estimate of the gyro biases. In order to further reduce the cost of this attitude system, an offshoot was created with a single GPS baseline for yaw, with roll and pitch obtained by a non-linear acceleration vector matching [64]. This work is further complemented by [65], where the use of magnetometers is offered as an alternative to the single GPS baseline for yaw. This can be seen as a precursor to the work contained in this thesis, with the primary differences being a more formal mathematical basis and an integration of the magnetometer triad during accelerated motion.

Vector matching in multiple coordinate frames is often referred to as Wahba’s problem. First published in 1965 [144], Wahba proposed an attitude solution by matching two non-zero, non-colinear vectors that are known in one coordinate frame, and measured in another. Several solutions to this method of attitude determination have been proposed and implemented [10], [11], [73], usually on satellites with star-tracker sensors. In this

chapter, a novel method of solving Wahba's problem is demonstrated, in which the measurement equation can be cast into a standard form. By using the quaternion representation of attitude, the algorithm does not require the solution of transcendental equations (as would be the case with Euler angles) and is suitable for implementation in a small, inexpensive microcomputer. Specifically, by measuring the body-fixed magnetic field and the body-fixed gravitational acceleration, the attitude of a moving object is tracked both in simulation, and experimentally with post-processed data.

SECTION 4.1 MOTIVATIONS

The need for a complete three-axis attitude reference unit on a marine surface vessel is not immediately obvious. However, there are a few pressing reasons apparent upon closer examination. Since heading is sensed magnetically, the roll and pitch can alter the measured heading by as much as 10-15 degrees under normal operating conditions. This is due to the downward component of the magnetic field (dip) corrupting the horizontal components of the measurement. This precludes accurate heading information which is a requirement for high precision control. Further discussion can be found in Chapter 6.

The other motivation comes from the unique lever arm problems associated with GPS control of a marine vessel. Ideally, the GPS antenna would be placed on the highest point of the craft, yielding an unobstructed view of the sky. This would give the best view of the satellites and minimize multipath effects. However, the point of the vessel that needs to be controlled, and hence its position and velocity sensed, is the center of mass of the vessel. Only on a simple point mass do the center of mass and the highest point coincide. Thus, the position of the center of mass will always be the sensed position of the antenna corrected for some lever arm position. In the case of a sail-propelled vehicle, the ideal location for the GPS antenna is at the top of the mast.

A synthetic sensor is created by fusing the GPS position data with the known lever arm and attitude data to place a virtual antenna at the center of mass of the vehicle, which can be below structures that would normally obstruct the GPS signal and can even be below the water. Without this synthetic sensor, roll and pitch of the vessel in waves can cause the antenna to swing with the mast. This creates phantom inputs into the control algorithm that would lead the boat to turn into the heel, further exacerbating the problem. Furthermore, this can make a non-minimum phase situation occur where control inputs first cause a direct excursion from the desired control path. Non-minimum phase systems possess the disadvantage that optimal control methods are always band-limited due to initial response in the wrong direction.

SECTION 4.2 REFERENCE FRAME REVIEW

The attitude of a vehicle is the difference between the navigation frame, usually fixed to Earth at the location of the vehicle in a traditionally North-East-Down coordinate system, and a coordinate frame fixed to the body of the vehicle (Figure 4-1). Traditionally, the body frame has the x-axis pointed out the nose of the vehicle, the y-axis out the right side, and the z-axis down.

Specifically, attitude describes the relative orientation of two (usually orthogonal) unit vector triads. The attitude simply describes what rotations one must perform to move from one description to the other. The reference frame and body frame are used to define a reference attitude to call zero on the various parameterizations. For instance, traditionally, the North-East-Down (NED) reference frame attached to Earth is considered as the inertial frame. While this works perfectly well for an aircraft flying a few hundred miles, this frame quickly loses its utility as a reference if the object of interest were a satellite. For a satellite, one might desire to know the attitude relative to a coordinate frame that tracks the

satellite and has its x-axis pointing along the orbit, its z-axis pointing towards the center of Earth, and the y-axis pointing out of the orbit plane.

Alternately, a coordinate frame that is attached to the center of Earth and points towards a distant star might be useful to measure effects on a satellite that is in a heliocentric orbit. This coordinate frame would be difficult to use for an interplanetary probe, which would probably be better served by a sun-fixed frame, pointing out towards galactic center.

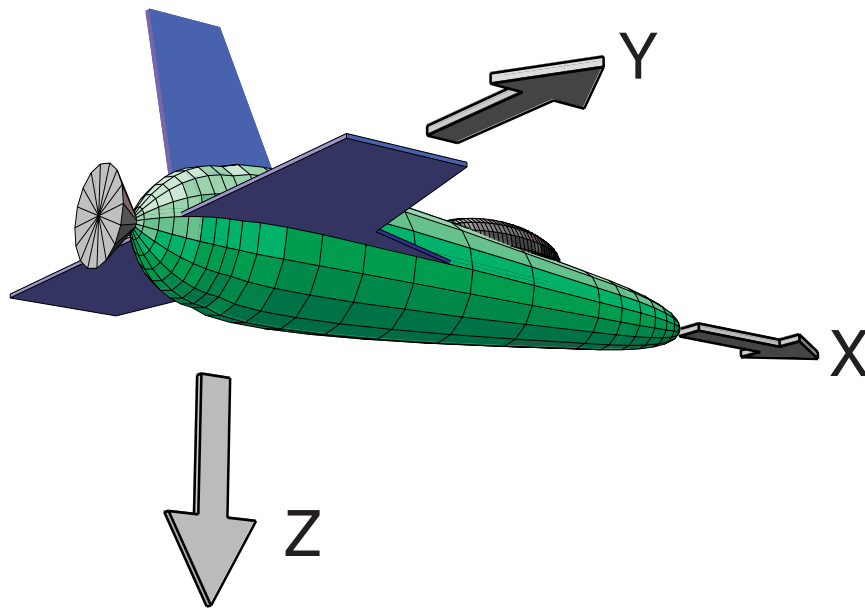


Figure 4-1 The body frame rigidly attached to the vehicle. This is the standard aircraft coordinate system definition. X-axis out the nose, Y-axis out the right wing, and Z-axis down. The body frame remains fixed with respect to the vehicle. Other frames are used as appropriate, for instance, an inertial frame attached to Earth, with its X-axis pointing North, Y-axis pointing East, and Z-axis pointing down. Transformations between these coordinate frames are used to keep values correct in their respective frames.

A reference frame is simply that: an orientation to call zero, something relative to which attitude may be measured. In the case of the attitude problem discussed here, it is convenient to use the North-East-Down frame and refer to this as the navigation frame. Reemphasizing, a body frame is used that is rigidly attached to the vehicle, with the x-axis

pointing out the nose, the y-axis out the right wing or starboard side, and the z-axis down (as shown in Figure 4-1).

SECTION 4.3 ATTITUDE PARAMETERIZATION

Having clarified that attitude is simply the relative orientation of one frame to another, there are several methods used for describing the relative orientation between frames. The three main parameterizations for attitude are: *Euler angles*, *Direction Cosine Matrix*, and *quaternions*. Several textbooks such as [86], [80], and [60], provide an excellent background that is reviewed here only for completeness.

Euler angles are the most intuitive parameterization. Three angles, yaw, pitch, and roll, are used to describe the attitude. Starting with the vehicle aligned to the navigation frame, the vehicle is first yawed about the z-axis, as in Figure 4-2 (top frame). Then the vehicle is pitched about the new body y-axis (Figure 4-2 middle frame), and finally the vehicle is rolled about the resulting x-axis (Figure 4-2 bottom frame). This is referred to as a [3-2-1] Euler angle set due to the order of rotation axes, and is made unique by limiting yaw to +/- 180 degrees, pitch to +/- 90 degrees, and roll to +/- 180 degrees.

The parameterization of attitude is used in equations to transform vector quantities from one coordinate frame to the other (the so-called transformation matrices), and in the propagation or integration of attitude based on some known or measured rotation rate. The generalized equations for a rigid spinning body, known as Euler's equations, are independent of parameterization of attitude, and are expressed as:

$$\frac{d}{dt}\omega = [I]^{-1}[M - [\omega \times]I\omega] \quad (\text{EQ 4.1})$$

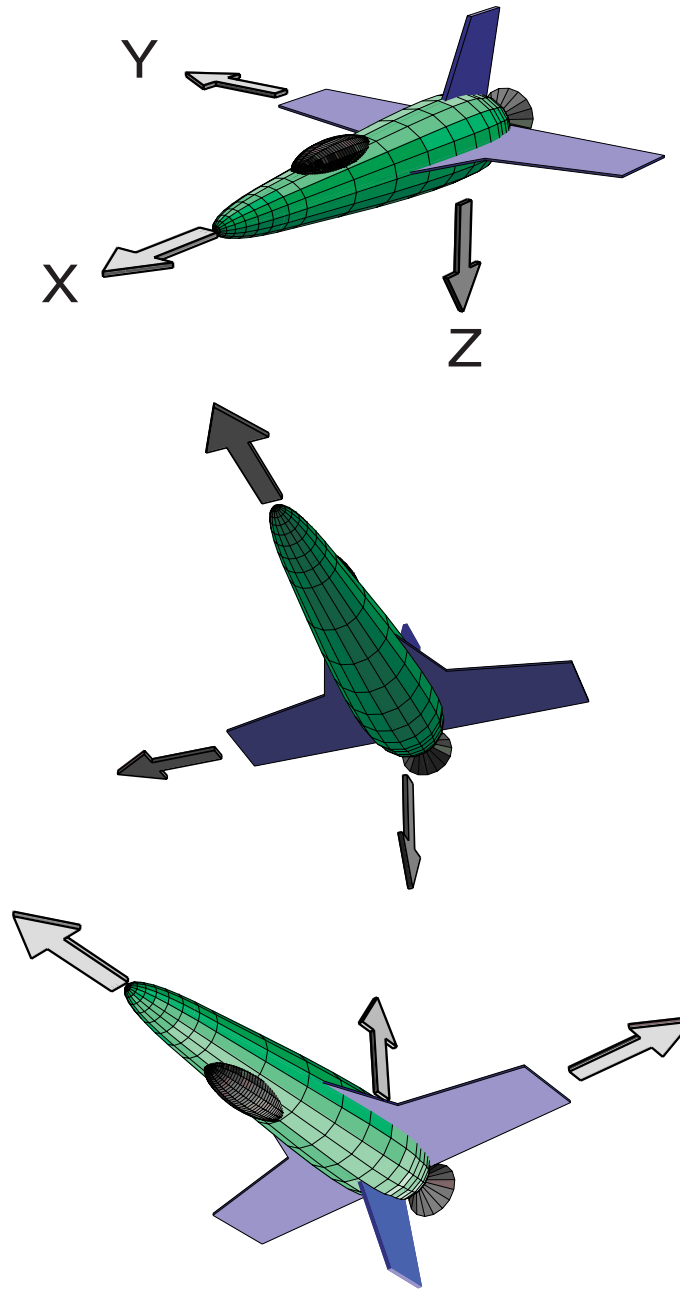


Figure 4-2 The Euler angle parameterization for attitude is usually defined as a [3-2-1] rotation. That is, first yaw (Ψ) about the navigation frame z-axis (top drawing), then pitch (Θ) about the intermediate frame y-axis, and finally roll (Φ) about the resulting body x-axis, to the final orientation.

where ω is the angular rate of the body, I is the moment of inertia matrix, and M is the applied external torque. The quantity $[\omega \mathbf{x}]$ is the cross-product matrix, defined as

$$[\omega \mathbf{x}] = \begin{bmatrix} 0 & -\omega_z & \omega_y \\ \omega_z & 0 & -\omega_x \\ -\omega_y & \omega_x & 0 \end{bmatrix} \quad (\text{EQ 4.2})$$

The transformation matrix from navigation to body coordinates, expressed as a function of Euler angles is:

$$\mathbf{C}^{n \rightarrow b} = \begin{bmatrix} \cos \psi \cos \theta & \sin \psi \cos \theta & -\sin \theta \\ -\sin \psi \cos \theta + \cos \psi \sin \theta \sin \phi & \cos \psi \cos \theta + \sin \psi \sin \theta \sin \phi & \cos \theta \sin \phi \\ \sin \psi \sin \theta + \cos \psi \sin \theta \cos \phi & -\cos \psi \sin \theta + \sin \psi \sin \theta \cos \phi & \cos \theta \cos \phi \end{bmatrix} \quad (\text{EQ 4.3})$$

where the angles are yaw (ψ), pitch (θ), and roll (ϕ). The propagation equation for the time rate of change of Euler angles with the body rates as inputs is:

$$\frac{d}{dt} \begin{bmatrix} \phi \\ \theta \\ \psi \end{bmatrix} = \begin{bmatrix} 1 & 0 & -\sin \theta \\ 0 & \cos \phi & \sin \phi \cos \theta \\ 0 & -\sin \phi & \cos \phi \cos \theta \end{bmatrix}^{-1} \begin{bmatrix} \omega_x \\ \omega_y \\ \omega_z \end{bmatrix} \quad (\text{EQ 4.4})$$

where

$$\begin{bmatrix} \omega_x \\ \omega_y \\ \omega_z \end{bmatrix} = \begin{bmatrix} p \\ q \\ r \end{bmatrix} \quad (\text{EQ 4.5})$$

and p , q , and r are the body fixed rotation rates as measured by on-board gyroscopes.

There are several advantages to Euler angles. They are immediately intuitive and an efficient method of parameterizing attitude. Furthermore, the angles are typically a required output of an attitude system. However, in order to transform a vector from one frame to another, a Direction Cosine Matrix (DCM) must be formed from the Euler angles and that DCM is full of transcendental functions as demonstrated in Equation 4.3. Also, when integrating the Euler angles to propagate attitude using a known or measured rota-

tion rate, the resulting equations are highly non-linear and again full of transcendental functions (Equation 4.4). Lastly, there is an ambiguity when the pitch angle is at either +/- 90 degrees. In a mathematical sense, there is a singularity, and yaw and roll cannot be defined, though the sum of yaw and roll and their difference remain well behaved. This is known as “Gimbal Lock” and in the days of mechanical gyroscopes was a concern for attitude system designers.

Another method for parameterizing attitude is through the DCM directly. The DCM is the transformation matrix between the navigation and body frames and thus is almost always in a form needed for further computation. The DCM is an orthonormal matrix, meaning that its transpose and its inverse are the same, and each of its columns is the unit normal basis vector of the navigation frame expressed in body coordinates.

The time propagation equation for the DCM can be written as:

$$\frac{d}{dt} \mathbf{C}^{n \rightarrow b} = -[\omega \mathbf{X}] \mathbf{C}^{n \rightarrow b} = \begin{bmatrix} 0 & \omega_z & -\omega_y \\ -\omega_z & 0 & \omega_x \\ \omega_y & -\omega_x & 0 \end{bmatrix} \mathbf{C}^{n \rightarrow b} \quad (\text{EQ 4.6})$$

where again,

$$\begin{bmatrix} \omega_x \\ \omega_y \\ \omega_z \end{bmatrix} = \begin{bmatrix} p \\ q \\ r \end{bmatrix} \quad (\text{EQ 4.7})$$

and p , q , and r are the body fixed rotation rates.

The clear advantage of the DCM is that the transformation matrix is already formed and the time propagation equation is a straightforward function with no transcendental functions or other obvious problems. The disadvantages are threefold. First, the DCM has no intuitive value whatsoever and discerning the rotation via the DCM is difficult at best. Second, the time propagation equation only contains three equations but the

DCM contains nine unique elements. The remaining six equations come from the constraint equations governing an orthonormal DCM. That is, the DCM must have its inverse equal to its transpose and each of its rows and columns must have unit length. These equations are non-linear and require much additional computation to resolve. In practice, this means that due to numerical instability during integration, the DCM must be constantly re-normalized and re-orthogonalized. This adds computational overhead, and often gives poor results if the integration is allowed without the re-normalization. Finally, there is a certain inelegance in carrying around nine parameters to describe only three angles.

The last parameterization discussed in this thesis is quaternions. Quaternions arise from the observation that any rotation between two coordinate frames can be recast as a single rotation about some unit vector. Thus quaternions represent the axis and angle of rotation between the navigation and body frames. The history and practical use of quaternions is discussed at length in Section 4.4 on page 102. The advantages of quaternions are efficiency (four parameters versus nine in the DCM), and the fact that both transformation and time propagation equations remain linear and computationally easy (requiring only simple addition and multiplication functions).

The transformation of a vector quantity from the navigation- to the body-frame can be accomplished with two quaternion multiplications:

$$r_n = q \otimes \begin{bmatrix} 0 \\ r_b \end{bmatrix} \otimes q^* \quad (\text{EQ 4.8})$$

where q is the base quaternion, and q^* is the quaternion's complement. The vector, r , is some arbitrary vector expressed in the navigation and body frames as denoted by the subscript n or b , respectively.

Likewise, the time propagation equations are equally simple:

$$\frac{d}{dt}q = -\frac{1}{2}\Omega q \quad (\text{EQ 4.9})$$

where Ω is defined as:

$$\Omega = \begin{bmatrix} 0 & -\omega_x & -\omega_y & -\omega_z \\ \omega_x & 0 & \omega_z & -\omega_y \\ \omega_y & -\omega_z & 0 & \omega_x \\ \omega_z & \omega_y & -\omega_x & 0 \end{bmatrix} = \begin{bmatrix} 0 & -\omega^T \\ \omega & [\omega \times] \end{bmatrix} \quad (\text{EQ 4.10})$$

where ω is again,

$$\begin{bmatrix} \omega_x \\ \omega_y \\ \omega_z \end{bmatrix} = \begin{bmatrix} p \\ q \\ r \end{bmatrix} \quad (\text{EQ 4.11})$$

and the rotation rates are body-fixed.

Thus the time propagation matrix, Ω is simply the assembly of the ω , the cross-product matrix of ω and the transpose of ω

Again, the lack of intuition with quaternions is a disadvantage. In and of itself, an axis and angle representation is intuitive, but neither the axis nor the angle are immediately obvious from an initial inspection of the quaternion. Quaternions are, however, efficient, have no singularities, and are easily implemented on a digital computer without the need for transcendental functions. The attitude system assembled for the Atlantis was implemented using the quaternion attitude estimation algorithm developed in this chapter.

Essentially, the choice of parameterization is driven by the requirements of the system. If most of the attitude computation is integration or propagation, quaternions have an advantage. However, if the integration times are short, or the output is used by a human, then the quaternions would have to be converted to Euler angles to be useful, and thus

there is an advantage to remaining with the Euler angle parameterization in this case. Lastly, “gimbal lock” is not a problem with modern electronics, and can be dealt with by the use of some simple switching logic in the software.

SECTION 4.4 QUATERNION REVIEW

Quaternions are actually hyper-complex numbers of rank four and were invented by Sir William Rowan Hamilton in 1848. He was working on extending the simple complex number to have a vector imaginary part, as opposed to a mere scalar. The quaternion, along with the operations of quaternion addition and multiplication, forms a non-commutative division ring [86]. Though the application of this system of mathematics eluded his lifetime, the properties of the quaternion math are wonderfully adept at rotations, transformations, and keeping track of attitude. Specifically, quaternion math permeates the fields of satellite attitude control and computer graphics.

The quaternion is an “axis and angle” representation of the rotation between two coordinate frames. That is, the vector part of the quaternion can be seen to indicate an axis about which the object is rotated, and the scalar part the magnitude of that rotation. Mathematically, this can be seen from the properties of the DCM or transformation matrix:

$$tr[\mathbf{C}^{n \rightarrow b}] = 1 + 2 \cos \Phi \quad (\text{EQ 4.12})$$

where tr is the trace operator, and Φ is the total angle between the two frames. Also,

$$\frac{\mathbf{C}^{n \rightarrow b} - (\mathbf{C}^{n \rightarrow b})^T}{2} = \sin \Phi \begin{bmatrix} 0 & a_z & -a_y \\ -a_z & 0 & a_x \\ a_y & -a_x & 0 \end{bmatrix} = -[a \times] \sin \Phi \quad (\text{EQ 4.13})$$

where a is the unit vector about which the frame rotates the total angle, Φ , to become the second frame. Intuitively, this can be visualized with the following thought experiment:

visualize the human right hand with the index finger pointing straight out, the thumb up, and the second finger bent at the top knuckle so as to point to the left. This defines the unit triad. Notice that almost any two orientations can be accomplished by bending the wrist and rotating the entire arm at the elbow. Realize that this is a single rotation about some strange axis. Thus, any rotation can be converted to a single rotation about some (arbitrary) axis. With this in mind, the definition of the quaternion as a representation or parameterization of attitude is shown:

$$q = \begin{bmatrix} \cos \frac{\Phi}{2} \\ a_x \sin \frac{\Phi}{2} \\ a_y \sin \frac{\Phi}{2} \\ a_z \sin \frac{\Phi}{2} \end{bmatrix} = \begin{bmatrix} q_0 \\ \vec{q} \end{bmatrix} \quad (\text{EQ 4.14})$$

Because the rotation can be positive about the vector, a , or negative about the opposite vector, $-a$, the quaternion is unchanged by sign. Thus, in terms of attitude:

$$q = -q \quad (\text{EQ 4.15})$$

Likewise, in order for the quaternion to represent attitude, it must be a unit length quaternion, or:

$$q^T q = q q^T = 1 \quad (\text{EQ 4.16})$$

which can be verified by substituting the base formulation of the quaternion, Equation 4.14, into this equation. The quaternion complement, or inverse, represents a reverse rotation from the one specified. As can be seen from substituting $-\Phi$ for Φ in Equation 4.14,

$$q^{-1} = q^* = \begin{bmatrix} q_0 \\ -\vec{q} \end{bmatrix} = \begin{bmatrix} -q_0 \\ \vec{q} \end{bmatrix} \quad (\text{EQ 4.17})$$

The last two basic quaternion math requirements are for multiplication and transformation. The quaternion multiplication represents successive rotation in *reverse* order of multiplication, thus $q \otimes s$ represents first a rotation through the quaternion, s , and then further rotation through the quaternion, q . The vector equation for quaternion multiplication is:

$$r = q \otimes s = \begin{bmatrix} q_0 s_0 - (\vec{q} \cdot \vec{s}) \\ q_0 \vec{s} + s_0 \vec{q} + \vec{q} \times \vec{s} \end{bmatrix} \quad (\text{EQ 4.18})$$

which can also be written as:

$$q \otimes s = \left(q_0 I + \begin{bmatrix} 0 & -\vec{q}^T \\ \vec{q} & [\vec{q} \times] \end{bmatrix} \right) s \equiv [Q_+(q)]s \quad (\text{EQ 4.19})$$

or alternately as:

$$q \otimes s = \left(s_0 I + \begin{bmatrix} 0 & -\vec{s}^T \\ \vec{s} & [-\vec{s} \times] \end{bmatrix} \right) s \equiv [Q_-(s)]q \quad (\text{EQ 4.20})$$

where I is the $[4 \times 4]$ identity matrix. As previously stated, the quaternion multiplication and inverse properties can also be used to transform a vector quantity into a new coordinate frame:

$$r_n = q \otimes \begin{bmatrix} 0 \\ r_b \end{bmatrix} \otimes q^* \quad (\text{EQ 4.21})$$

The transformation matrix can then be written as:

$$\overset{n \rightarrow b}{C} = \begin{bmatrix} 2q_0^2 + 2q_1^2 - 1 & 2q_1q_2 - 2q_0q_3 & 2q_1q_3 + 2q_0q_2 \\ 2q_1q_2 + 2q_0q_3 & 2q_0^2 + 2q_2^2 - 1 & 2q_0q_1 - 2q_2q_3 \\ 2q_1q_3 - 2q_0q_2 & 2q_0q_1 + 2q_2q_3 & 2q_0^2 + 2q_3^2 - 1 \end{bmatrix} \quad (\text{EQ 4.22})$$

or, in matrix form:

$$\overset{n \rightarrow b}{C} = (2q_0^2 - 1)I - 2q_0[\vec{q} \times] + 2\vec{q}\vec{q}^T \quad (\text{EQ 4.23})$$

These equations provide all of the necessary tools to derive the attitude algorithm, and will be used in later sections to demonstrate the quaternion estimation of Wahba's problem. For completeness, the transformation from quaternions to Euler angles is also included:

$$\Psi = \operatorname{atan} \frac{2q_1q_2 + 2q_0q_3}{2q_0^2 + 2q_1^2 - 1} \quad (\text{EQ 4.24})$$

$$\Theta = \operatorname{asin}(2q_0q_2 - 2q_1q_3) \quad (\text{EQ 4.25})$$

$$\Phi = \operatorname{atan} \frac{2q_2q_3 + 2q_0q_1}{2q_0^2 + 2q_3^2 - 1} \quad (\text{EQ 4.26})$$

these are often required when the output of the attitude system is used directly by a human operator.

SECTION 4.5 VECTOR MATCHING

In 1965, Grace Wahba proposed that given a minimum of two vector measurements in the body frame, and a known value for the vectors in the reference frame, then the rotation between the body frame and the reference frame can be uniquely determined as long as the vectors are non-colinear and of non-zero length [144]. Another way of stating this is that a (non-orthogonal) triad can be formed by each of the two vectors and the cross-product between the two. With measurements of the components of the two vectors, the rotation necessary to force the vectors in line with this triad can be computed. The necessity of a non-zero value for the cross-product forces the two vectors to be non-colinear, and of non-zero length. If only one vector is present, the rotation can only be resolved to two of the necessary three angles.

Wahba's problem, as vector matching has become known, is used on many satellites for attitude information. The sensors are usually high quality star trackers that give

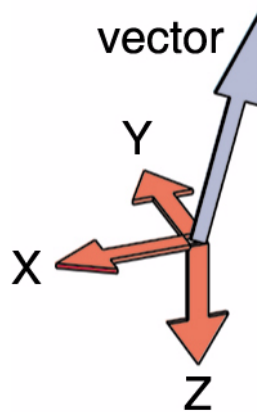


Figure 4-3 A vector is shown in the inertial coordinate frame. This will be the basis for an example of the mechanics of Wahba's problem and how it is solved. The blue vector can be any vector quantity that is known in the inertial frame, such as magnetic field or the acceleration of gravity.

measurements to the line-of-sight of known stars. Often, these are complemented with high-quality gyroscopes in order to smooth the attitude solution.

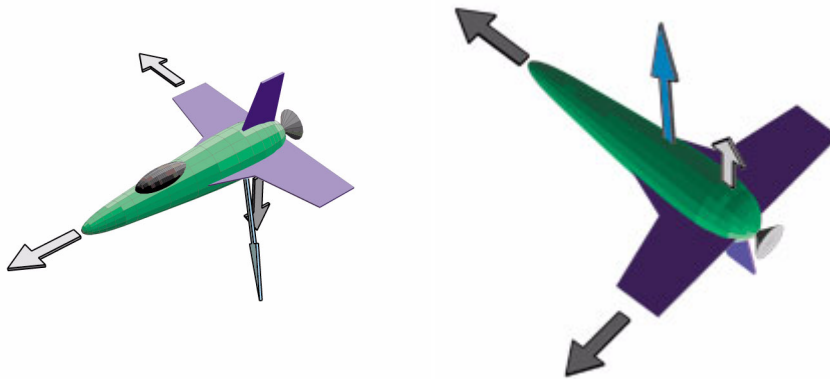


Figure 4-4 The same vector as previously defined in the inertial frame, as measured in the body coordinates (on the left side). In order to line up the vector to the inertial "known" state, the body must be rotated to line the vector up. This rotation is exactly that which transforms body quantities to inertial quantities. Of course, with only one vector, there remains an ambiguity of rotation about the vector itself. Thus, two or more non-colinear vectors are required.

Visually, the solution to Wahba's problem is simple. Examine the triad and vector pictured in Figure 4-3. The blue vector is some quantity that is known in the inertial coor-

dinate frame. Measuring the same components of that vector in the body frame, rotate the body until the vector lines up with what it is known to be in the inertial coordinates. At this point, the rotation is exactly that which transforms a quantity from the body to the inertial frame. This is pictured in Figure 4-4.

Several different algorithms have been used to solve Wahba's problem. Most notable are the papers by Bar-Itzhack [9], [10], [11], [12], and [13], Creamer [35], Lefferts [87], and Markley [95], [96]. These authors present algorithms that use singular value decompositions and other advanced matrix techniques to solve directly for the rotation matrix. The method used in this thesis is different from all of them and will be developed in detail in the following section.

SECTION 4.6 GYROSCOPE-FREE ATTITUDE ESTIMATION

In order to minimize the cost of the attitude system for the Atlantis project, it was decided not to include gyroscopes in the attitude solution. Two things make this reasonable. First, the bandwidth requirement for attitude was fairly low, at 10 Hz; and second, the rotation rates expected from the Atlantis during her trial runs were expected to be very small.

The vector matching algorithm, as previously explained, requires two non-colinear, non-zero length vectors in order to function. For convenience, the vectors used were Earth's magnetic field and total gravitational acceleration. Earth's magnetic field has been extensively mapped and the gravitational field can be assumed to point straight down.

In order to measure the body-fixed components of the magnetic field, a three-axis strap-down magnetometer was used. Body fixed acceleration was measured by a triad of micromachined accelerometers. The accelerometers, however, do not measure gravity

directly. Instead, they measure the specific force acting upon them. In this case, this means that they measure the vector difference of any acceleration in the inertial frame and gravity. Thus, the specific force in the navigation frame, i.e., the acceleration of the vehicle minus gravity must be known.

$$\dot{\vec{f}} = \dot{\vec{a}} - \dot{\vec{g}} \quad (\text{EQ 4.27})$$

In an aircraft, as later examples will demonstrate, the inertial acceleration is estimated using the difference in subsequent GPS velocity measurements divided by the time elapsed between measurements (numerical differentiation of velocity to yield acceleration). This provides a good estimate of inertial acceleration, but the accuracy degrades as velocity decreases. This is due to the fact that the noise on the GPS velocity measurement is constant. As the velocity decreases, the portion of the measurement that is noise increases (decreasing signal to noise ratio). At very low velocities, it is unclear if the object is in motion or the output is noise from the GPS signal. This is further exacerbated by the differencing of subsequent measurements to generate a pseudo-derivative. As the noise is white, subtraction cannot be assumed to cancel the noise. In the specific case of the Atlantis, the accelerations were so small that the noise in the GPS velocity measurement was far larger than the signal being estimated. Thus, in the actual Atlantis hardware, the GPS acceleration was not used. The Atlantis was assumed to be accelerating at such a small fraction of one g that this omission caused only minor errors.

SECTION 4.6.1 MATHEMATICAL FORMULATION

The development of the novel attitude algorithm is straight forward and concludes with the attitude problem recast into a standard form to which most of the conventional filtering tools can be applied.

First, assume that the vector measurements are known in the navigation frame (denoted by the superscript n), and measured in the body frame (denoted by the superscript b). Thus, the magnetic field in the navigation frame is denoted as M^n and the magnetic field measured in the body frame is denoted as M^b .

The problem is one of attitude estimation in the quaternion domain. Thus there are three quaternions required: the true quaternion, q_{true} , the estimated attitude quaternion, \hat{q} , and the error quaternion relating the previous two, q_e . The relationship between the three is:

$$q_{true} = q_e \otimes \hat{q} \quad (\text{EQ 4.28})$$

Thus the estimated attitude is again rotated slightly more by the error quaternion to become the true quaternion. In a conventional sense, q_e might be referred to as a correction quaternion rather than an error quaternion, but in order to remain consistent with prior research in [35], [43], and [126], it is defined here as the error quaternion. Note that because the error quaternion, q_e , is small, it can be approximated as:

$$q_e \equiv \begin{bmatrix} 1 \\ \vec{q}_e \end{bmatrix} \quad (\text{EQ 4.29})$$

where the scalar part of the quaternion is set to one. Note also that this is consistent with both the definition found in Equation 4.14 and the assumption that the angle of rotation, Φ , is small.

The first part of the mathematical formulation will focus on the magnetic field with the understanding that the same exact formulation applies to the total acceleration. The use of magnetic field is entirely arbitrary and was done because a convenient sensor was available in this problem. The formulation will remain correct for any vector quantity that can be known in the navigation frame and measured in the body frame.

The attitude formulation begins with a simple transformation of a vector from the body frame to the navigation frame:

$$\vec{M}^n = {}^{n \rightarrow b} \mathbf{C} \vec{M}^b \quad (\text{EQ 4.30})$$

or, in the quaternion domain:

$$\begin{bmatrix} 0 \\ \vec{M}^n \end{bmatrix} = q_{true} \otimes \begin{bmatrix} 0 \\ \vec{M}^b \end{bmatrix} \otimes q_{true}^* \quad (\text{EQ 4.31})$$

substituting in the definition of q_{true} from Equation 4.28,

$$\begin{bmatrix} 0 \\ \vec{M}^n \end{bmatrix} = (q_e \otimes \hat{q}) \otimes \begin{bmatrix} 0 \\ \vec{M}^b \end{bmatrix} \otimes (q_e \otimes \hat{q})^* \quad (\text{EQ 4.32})$$

which can be expanded to:

$$\begin{bmatrix} 0 \\ \vec{M}^n \end{bmatrix} = q_e \otimes \left(\hat{q} \otimes \begin{bmatrix} 0 \\ \vec{M}^b \end{bmatrix} \otimes \hat{q}^* \right) \otimes q_e^* \quad (\text{EQ 4.33})$$

where the center part, the transformation of the body-fixed magnetic field into the navigation frame via the estimate of the true attitude, is referred to as \hat{M}^n , i.e.,

$$\begin{bmatrix} 0 \\ \hat{M}^n \end{bmatrix} \equiv \left(\hat{q} \otimes \begin{bmatrix} 0 \\ \vec{M}^b \end{bmatrix} \otimes \hat{q}^* \right) \quad (\text{EQ 4.34})$$

\hat{M}^n is the estimate of the magnetic field expressed in the navigation frame. Making this substitution for \hat{M}^n :

$$\begin{bmatrix} 0 \\ \vec{M}^n \end{bmatrix} = q_e \otimes \begin{bmatrix} 0 \\ \hat{M}^n \end{bmatrix} \otimes q_e^* \quad (\text{EQ 4.35})$$

Note that using the transformation matrix or DCM notation, Equation 4.35 can be rewritten as:

$$\vec{M}^n = \vec{C}_{(q_e)}^{b \rightarrow n} \hat{M}^n \quad (\text{EQ 4.36})$$

Substituting Equation 4.23 for the DCM, transposing the equation to change from body to navigation, using the definition of q_e provided in Equation 4.29, and discarding the higher order terms, consistent with the assumption of a small vector portion of the error quaternion yields,

$$\vec{M}^n = (I + 2[\vec{q}_e \times]) \hat{M}^n \quad (\text{EQ 4.37})$$

which can be rearranged as:

$$\underbrace{\vec{M}^n - \hat{M}^n}_{\delta \vec{M}^n} = 2[\vec{q}_e \times] \hat{M}^n \quad (\text{EQ 4.38})$$

with the left hand side of Equation 4.38 denoted as $\delta \vec{M}^n$. Using the property of cross products that $A \times B = -B \times A$, and applying this to the right hand side of the equation:

$$\delta \vec{M}^n = -2[\hat{M}^n \times] \vec{q}_e \quad (\text{EQ 4.39})$$

Note that Equation 4.39 has the form of the standard measurement equation of:

$$z = Hx \quad (\text{EQ 4.40})$$

where, including the terms from the total acceleration:

$$z = \begin{bmatrix} \delta \vec{M}^n \\ \delta \vec{A}^n \end{bmatrix} \quad (\text{EQ 4.41})$$

and

$$H = \begin{bmatrix} -2[\hat{M}^n \times] \\ -2[\hat{A}^n \times] \end{bmatrix} \quad (\text{EQ 4.42})$$

and x is, of course, the vector portion of the error quaternion, \vec{q}_e .

Thus, the very non-linear equation for transforming a measured quantity from the body frame to a known quantity in the navigation frame has been recast in a standard form. The measurement, z , and the observation matrix, H , both change with every time step. This does not present a problem as standard time-varying linear solution schemes are well known.

SECTION 4.6.2 ITERATED LEAST SQUARES

One method of estimating the attitude quaternion from the development above is to use an iterated least squares. In this methodology, as soon as a measurement is recorded, the solution to the measurement equation is recomputed and the solution is “walked” into convergence. The steps for the iterated least squares solution are as follows:

- (1) Measure the body-fixed magnetic field and specific force: \vec{M}^b and \vec{A}^b .
- (2) Assume $\hat{q} = [1 \ 0 \ 0 \ 0]^T$ and $q_e = [1 \ 0 \ 0 \ 0]^T$.
- (3) Form the vector \hat{M}^n by quaternion multiplication: $\hat{M}^n = \hat{q} \otimes \vec{M}^b \otimes \hat{q}^*$.
- (4) Repeat Step (3) for \hat{A}^n .
- (5) Form the vector $\delta\vec{M}^b$ where $\delta\vec{M}^b = \vec{M}^b - \hat{M}^n$.
- (6) Repeat Step (5) for $\delta\vec{A}^b$.
- (7) Form the measurement vector, z , by stacking the results of Steps (5) and (6).
- (8) Form the observation matrix, H , as in Equation 4.42.
- (9) Form the pseudo-inverse of H , $H^\dagger = [H^T H]^{-1} H^T$.
- (10) Compute the new vector part of the error quaternion, $\vec{q}_e = \alpha [H^T H]^{-1} H^T z$.
- (11) Update the quaternion estimate: $\hat{q}(+) = q_e \otimes \hat{q}(-)$.
- (12) Return to Step (3) and repeat until converged.

The tuning parameter, α , in Step (10) is used to smooth the solution by using only part of the entire correction computed for the vector part of the error quaternion. The pseudo-inverse of H is invertible only when $\vec{M} \times \vec{A} \neq 0$, which mathematically restates the requirement that the two vectors be non-colinear and non-zero. To validate the algorithm, a Monte-Carlo simulation was performed where a random starting attitude was given to the algorithm. The body-fixed measurements were corrupted with appropriate levels of sensor noise, and the algorithm was allowed 100 iterations to converge with a tuning parameter, α , of 1/10. Figure 4-5 shows a time history for the attitude quaternion components during a single run in these series of simulations. As can be seen, the convergence to the correct attitude is rapid and smooth.

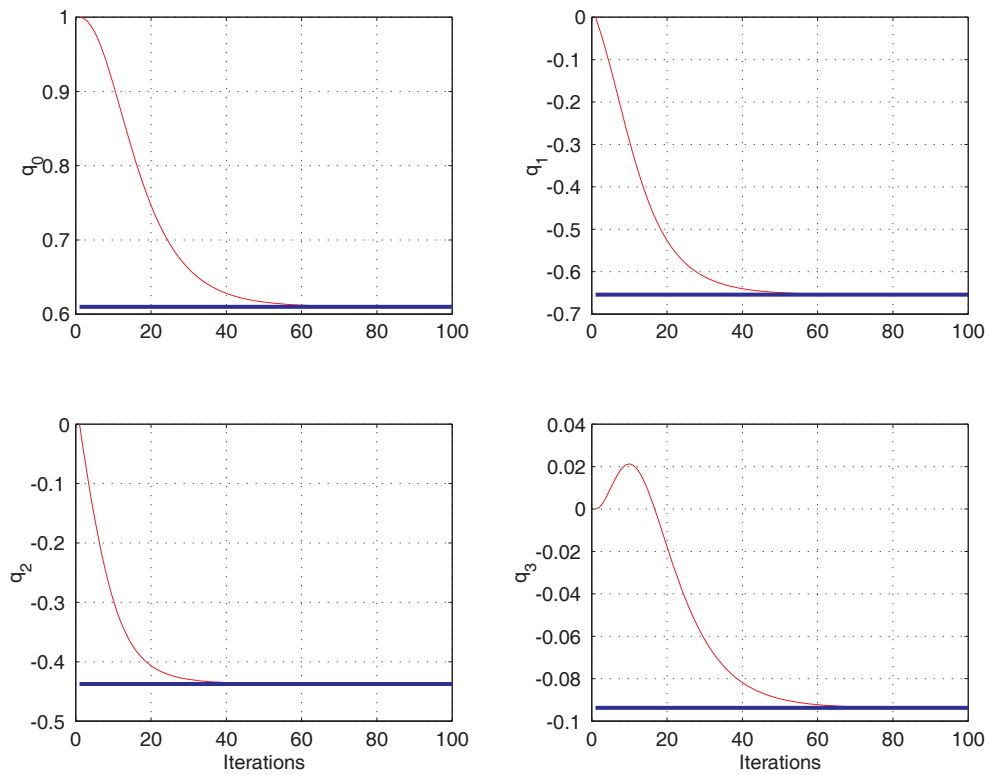


Figure 4-5 Quaternion convergence from Iterated Least Squares Monte-Carlo simulation. The body is set to a random orientation as indicated by the blue constant lines. The measured body fixed components of the magnetic field and gravity are calculated. The Iterated Least Squares algorithm is run for 100 times with a tuning parameter, α , of 1/10. Note that the solution is converged by 60 iterations.

In order to visualize the convergence of the algorithm, since the quaternions themselves do not lend an intuitive picture, a unit normal triad is attached to the simulated vehicle, and the trace of the tips of this triad plotted on the surface of a sphere. That is, the tip of a unit vector pointing out the nose of the aircraft is computed at every step in the iteration, and plotted on the surface of the sphere, along with the unit vector pointing out the right wing, and the one pointed down. That sphere, along with the traces, appears in Figure 4-6. The smoothness of the convergence is readily apparent in this view.

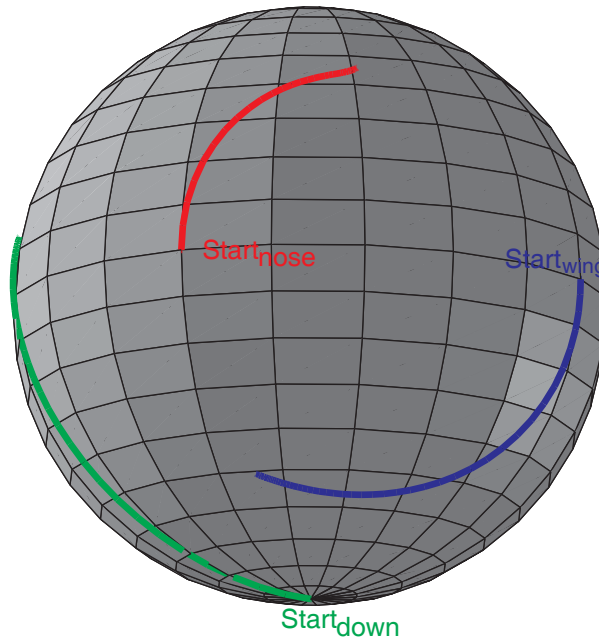


Figure 4-6 Iterated Least Squares solution convergence mapped onto a sphere. The orthogonal triad of unit vectors that point out the nose of the aircraft (in red), the right wing of the aircraft (in blue) and the bottom of the aircraft (in green) are rotated by the Iterated Least Squares algorithm at each step until convergence. Note that this algorithm is globally convergent.

The initial points, designated in red as “start nose,” in blue as “start wing,” and in green as “start down” correspond to the nose pointing north, and the aircraft level, as indicated by Step (2) of the iterated least squares algorithm, where $\hat{q} = [1 \ 0 \ 0 \ 0]^T$. The final

location of the three unit vectors is the true attitude. In order to see this more clearly, the sphere portrayed in Figure 4-6 is unwrapped into a Mercator projection in Figure 4-7, below.

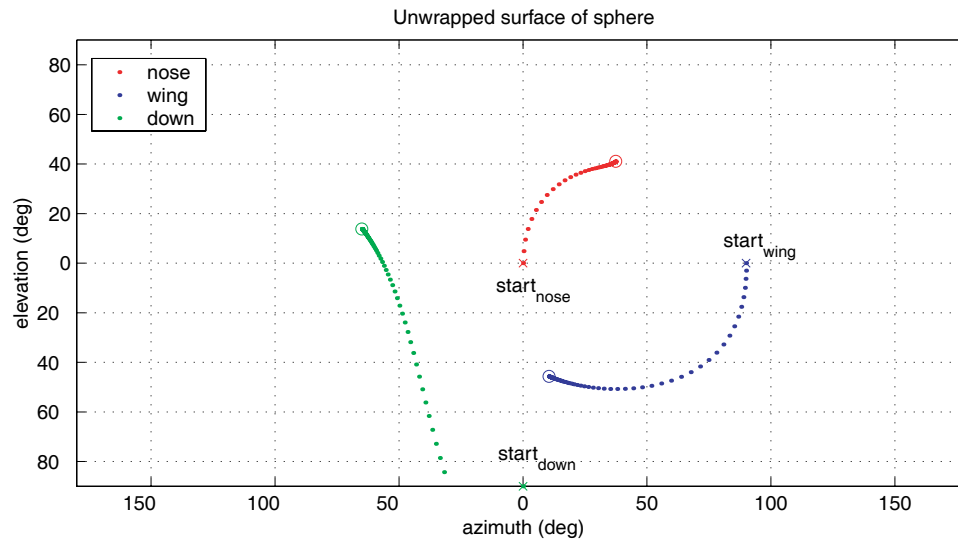


Figure 4-7 Iterated Least Squares solution sphere unwrapped via Mercator projection. Again, the unit normal triad of a unit vector out the nose of the aircraft (in red), out the right wing of the aircraft (in blue) and down through the bottom of the aircraft (in green) are plotted from the initial start of the Iterated Least Squares algorithm to convergence. Note that the initial large step in the down vector is an artifact of the unwrapping of the sphere into a rectangle.

The figures presented are of a typical run during the Monte-Carlo simulation. The iterated least squares quaternion estimation algorithm solution to Wahba's problem was numerically demonstrated to be globally convergent, in this static case, always converging to the correct attitude regardless of the initial guess on attitude. This was demonstrated by extensive simulation in which the true attitude was varied at 2.5 degree intervals through the entire space of possible attitudes. Furthermore, the tuning parameter is found to be quite robust, ensuring convergence to ε within n iterations as long as α is within the range of $[1/n \text{ to } 2]$.

SECTION 4.6.3 KALMAN FILTER

The iterated least squares solution works very well, but it is a snapshot solution based only on the current measurements of the vectors in the body frame. There is, however, more information available in the form of past attitude information. Typically, a Kalman filter is used to smoothly join the measurements with a dynamic model of the vehicle attitude. A Kalman filter is simply the linear-optimal estimator that minimizes the state error covariance for all time by properly blending prior information and current measurements. Certain assumptions about the broadband (white and Gaussian) nature of the model error (process noise) and sensor error (measurement noise) statistics are required for the optimality of the Kalman filter to hold.

In order to implement a Kalman filter, equations accounting for the dynamics must be included in the formulation. If angular rate measurements are available from gyroscopes, a dynamic model for the quaternion attitude estimate based on the kinematics of the attitude problem will be included [35]. If a dynamic model for the rate of change of the attitude quaternion is not included, then a lag will be introduced into the attitude solution. The lag, however, will be inconsequential if the dynamics are assumed to have a low frequency content. In this case, the quaternion errors may be modeled as an exponentially correlated or Gauss-Markov process. The dynamics of the state variable of interest, \hat{q}_e , can be written as:

$$\frac{d}{dt}\hat{q}_e = F\hat{q}_e + Gw \quad (\text{EQ 4.43})$$

where the state transition matrix, F , is:

$$F = -\frac{1}{\tau}I_{3 \times 3} \quad (\text{EQ 4.44})$$

and the noise input matrix, G , is:

$$G = -\tau F = I_{3 \times 3} \quad (\text{EQ 4.45})$$

and w is the white noise input and τ is the time constant of the exponential correlation.

If the problem is then formulated as a time-varying Kalman filter, using the state variable of interest and the measurements and measurement matrix as previously defined, the measurement update equation is stated as:

$$\hat{q}_e^{(+)} = \hat{q}_e^{(-)} + L(z - H\hat{q}_e^{(-)}) \quad (\text{EQ 4.46})$$

where the $(-)$ and $(+)$ superscripts denote before and after the measurement update, respectively. The measurement vector, z , is defined in Equation 4.41 and the measurement matrix is defined in Equation 4.42. The time-varying Kalman gain, L , is:

$$L = P^{(-)}H^T(H^TP^{(-)}H + R_v)^{-1} \quad (\text{EQ 4.47})$$

where P is the state error covariance matrix, and R_v is the measurement noise matrix. The time covariance propagation is carried out via:

$$P^{(+)} = \Phi P^{(-)}\Phi^T + C_d \quad (\text{EQ 4.48})$$

where Φ is the discrete equivalent of the state transition matrix, F , and C_d is the discrete process noise matrix. Finally, the measurement update of the covariance is carried out using the standard Kalman filter covariance update equation as found in [57]:

$$P^{(+)} = (I - LH)P^{(-)} \quad (\text{EQ 4.49})$$

Note that if gyroscopes are present, then Equation 4.43 through Equation 4.46 change substantially. A very complete treatment of gyroscope integration within the framework of quaternion attitude determination can be found in [56].

SECTION 4.6.4 SIMULATION RESULTS

To confirm the performance of the time-varying Kalman filter formulation, a simulation was performed. This simulation includes both attitude and gross motion dynamics, and is such that each Euler angle and velocity can be ascribed a sinusoidal function with

individual means, amplitudes, and frequencies. This allows the motion differentiation to yield the exact acceleration, which can then be corrupted by noise to simulate actual sensors.

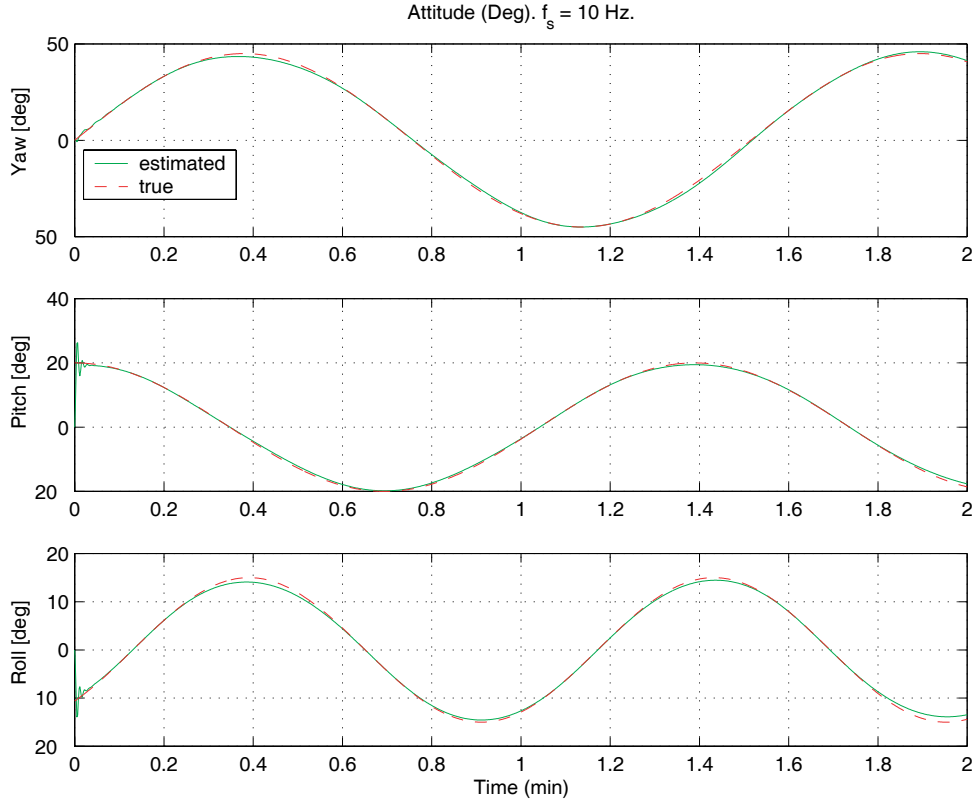


Figure 4-8 Simulation of the time-varying Kalman filter gyroscope-free attitude solution, in Euler angles. This is a model free Kalman filter solution that assumes the dynamics of the state transition matrix can be adequately modelled as a Gauss-Markov (exponentially correlated) process. Note the initial transients at the beginning as the filter converges on steady state gains.

Note that in this case, the accelerometers on board are not measuring gravity, but rather the vehicle specific force ($\vec{f} = \vec{a} - \vec{g}$). This is due to the fact that accelerations and gravitation cannot be distinguished as postulated by Einstein's equivalence principle. Thus, the local specific force is in fact, $\vec{a} - \vec{g}$, where both are expressed in the navigation frame. The local inertial acceleration, a , is obtained via differencing GPS velocity mea-

surements (in a numerical differentiation scheme). This has been included in the simulation.

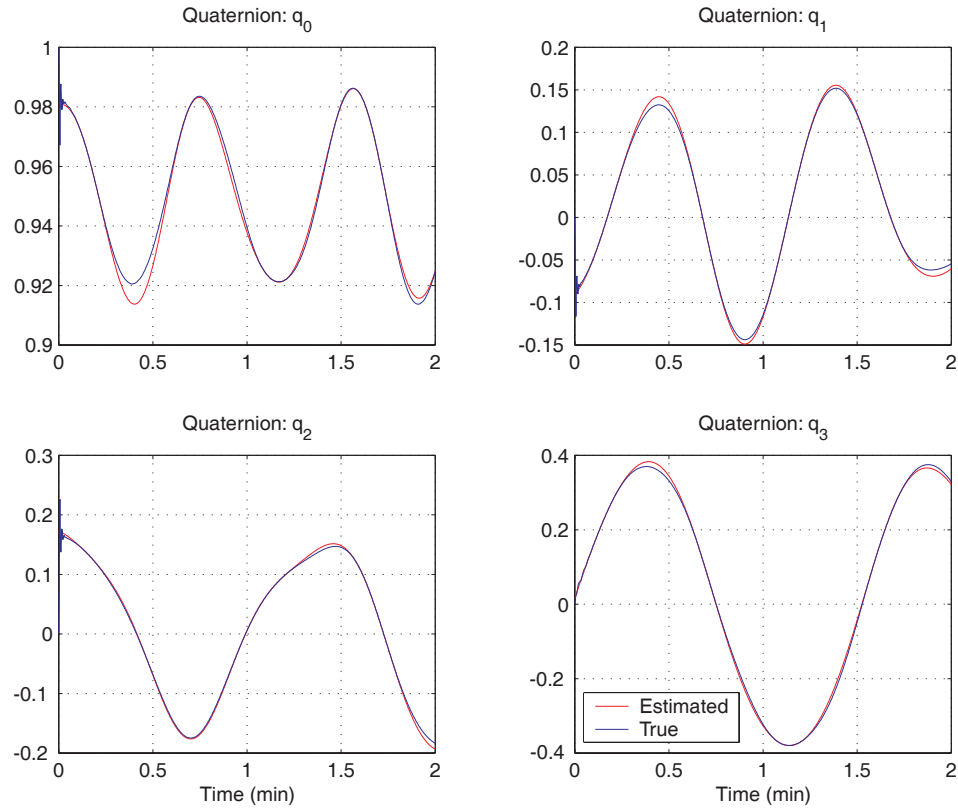


Figure 4-9 Simulation of the time-varying Kalman filter attitude solution, in quaternions. This is the same simulation as presented in the previous figure, but shown parameterized in quaternions. Again, note the initial transient response before the filter locks on to the steady state gains, and the small lag in the response at 0.4 minutes.

The simulation was run for approximately two minutes of simulated time, with the vehicle attitude oscillating back and forth. Figure 4-8 shows the three Euler angles, pitch, yaw, and roll, in degrees, with time along the x-axis. The initial transients show the filter locking on to the correct solution, and close inspection of the time around 0.4 minutes shows that the solution lags the true solution slightly at the inflection point of the roll and pitch motion.

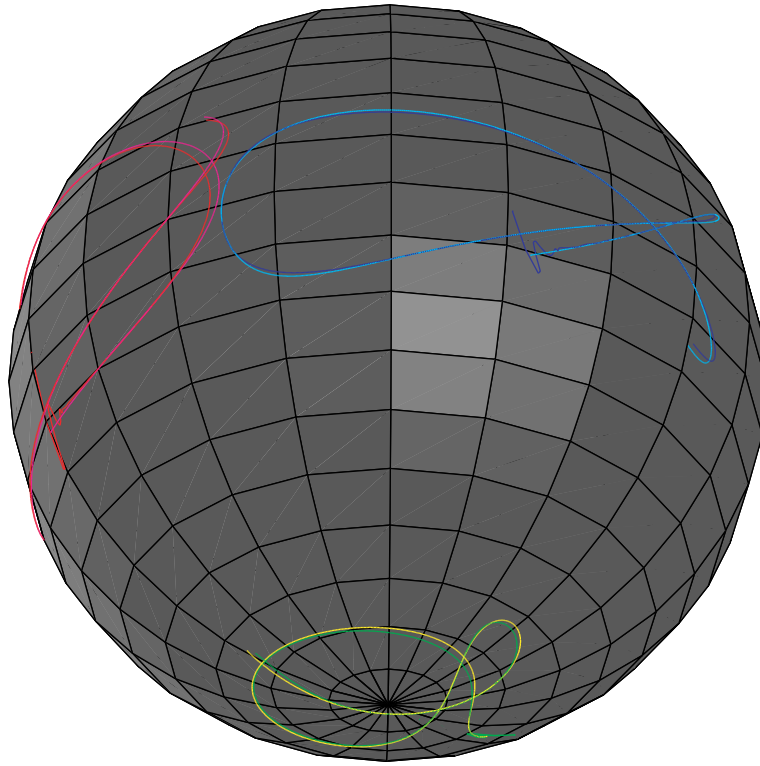


Figure 4-10 Simulation of the time-varying Kalman filter attitude solution, unit normal triad on sphere. In this figure, dynamic tracking (as opposed to a static solution) is shown. The true out the nose unit normal is shown in magenta, and the filtered version shown in red. The true out the right wing vector is shown in cyan, with the filtered version in blue, and the corresponding down vectors are in yellow and green.

Figure 4-9 shows the same simulation but in this case displaying the solution in the quaternion domain. The scalar part of the attitude quaternion estimate, \hat{q} , is placed in the upper left corner, with the three components of the vector portion shown. Since the quaternion has a scalar portion very close to one, the remaining vector components can be interpreted as the sine of roll, pitch, and yaw. Again, note the initial transient, and the lag at 0.4 minutes.

Figure 4-10 shows the trace of the estimated unit normal triad of the body-fixed axes on the surface of a sphere, along with the true attitude unit normal trace, for the same simulation. Here the transients of the initial convergence can be seen very clearly. This is

evidence that the estimator poles are fast, but lightly damped. Figure 4-11 shows the same information as Figure 4-10, but has unwrapped the surface of the sphere via a mercator projection. This projection distorts the areas near the top and bottom of the sphere, such that the information on the down axis is relatively poor, but the transients and lags show up very clearly on the nose and wing traces.

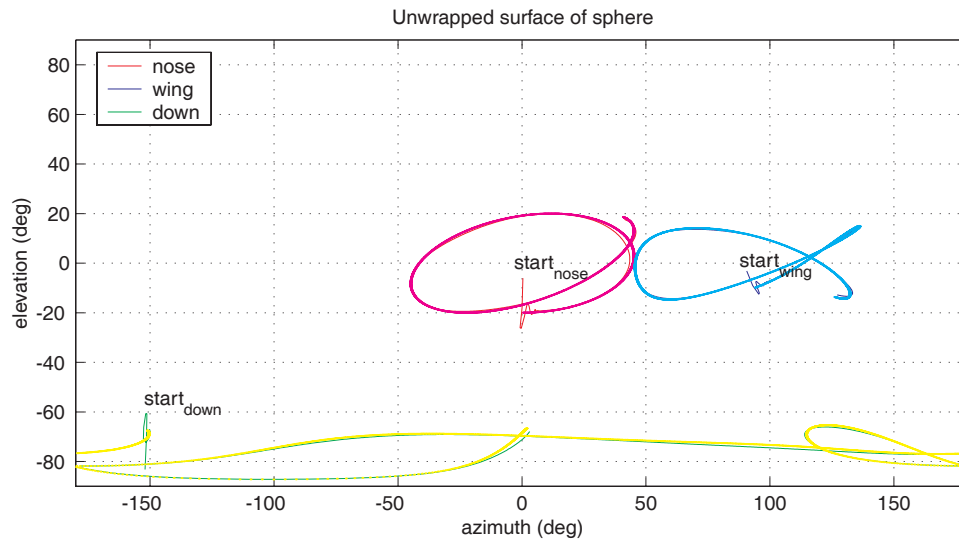


Figure 4-11 Simulation of the time-varying Kalman filter attitude solution, unit normal triad on sphere unwrapped using a mercator projection. This is the same data as the previous figure unwrapped. The large distortion on the “down” trace is due to the projection used. The initial transients and lag in the estimated attitude show up very well in the “nose” and “wing” traces.

The time-varying Kalman filter performs very well, even in the presence of gross sensor noise, and high frequency dynamics. The solution locks on to the true attitude quickly and demonstrates very little lag, in spite of the fact that the dynamic model is essentially a low-pass filter.

There is a trade-off in the tuning of the Gauss-Markov parameter, τ . A larger τ corresponds to longer correlation times and slows down the tracking response. This, however, also smooths the solution and effectively averages out noise. Decreasing τ improves tracking performance at the expense of making the solution more sensitive to noise. The initial

transients in the simulated response could be reduced greatly by initially using the static iterated least squares solution to begin the filter from a good initial guess of attitude.

SECTION 4.7 MAGNETOMETER CALIBRATION

In this application, one of the two known vectors for the vector matching algorithm is Earth's magnetic field. Driving this selection are the recent developments in materials technology that make low-cost three-axis strap-down magnetometers a reality. These sensors are, however, noisy and prone to both scale-factor and bias errors. Furthermore, the local magnetic field is corrupted by nearby objects. In this light, an introduction to the errors common to magnetometers and traditional methods for calibrating them will be presented, along with a novel two-step calibration algorithm.

SECTION 4.7.1 INTRODUCTION

Magnetometers are instruments used for measuring the strength and direction of magnetic fields. They are used extensively in aircraft navigation, marine navigation, and oilfield borehole applications. The magnetometers are used to determine the vehicle heading, where heading is defined as the angle formed between the longitudinal axis of the vehicle projected onto the horizontal plane and magnetic north. In most applications, normally a pair of magnetometers are mounted perpendicular to each other or a triad of magnetometers is mounted orthogonally. In this configuration, the magnetometers are used to measure the strength of Earth's magnetic field vector in body coordinates from which heading is computed. When the vehicle is straight and level (pitch and roll angles equal zero), magnetic heading is determined using:

$$\psi = \operatorname{atan}\left(\frac{B_x^b}{B_y^b}\right) \quad (\text{EQ 4.50})$$

where B_x^b and B_y^b represent measurements of Earth's magnetic field vector resolved in a coordinate system attached to the vehicle's body. The superscript "b" denotes a vector measurement made in the body coordinate frame. Errors in making the measurements B_x^b and B_y^b directly corrupt the accuracy of the heading obtained from Equation 4.50. The process of calibrating magnetometers involves identifying and removing the errors in these measurements. This section explores a novel method to calibrate these magnetometers.

SECTION 4.7.2 MAGNETOMETER MEASUREMENT ERROR MODELS

Magnetometers come in many different forms and operate on different principles. A new generation of low-cost magnetometers used in this research is Anisotropic Magneto-resistive (AMR) sensors. These units have a sensing element that is made from a nickel-iron alloy (or Permalloy) whose electrical resistance changes in the presence of magnetic fields. The Permalloy material is normally deposited on thin silicon wafers which can be bulk manufactured in a form suitable for commercial integrated circuit packages. The sensing element of the magnetometer used in this research has dimensions on the order of 10 mm per side [32]. The output of these devices is an analog voltage proportional to the strength of the magnetic field.

The mathematical model for the output of such a strap-down magnetometer triad is:

$$\hat{B}^b = C_m C_{sf} C_{si} (B^b + \delta B^b) \quad (\text{EQ 4.51})$$

where B^b represents the *actual* or true magnetic field vector while \hat{B}^b represents the *measured* magnetic field vector. The term δB^b represents the hard iron biases. The three leading matrices of the right-hand side of Equation 4.51 account for misalignment, scale factor errors, and soft iron, respectively.

The magnetic field that is used in heading determination is Earth's magnetic field. In most practical applications there will be other unwanted magnetic fields corrupting the measurements of the magnetometer triad. These unwanted fields are normally generated by ferromagnetic materials with permanent magnetic fields (or "hard irons") that are part of the aircraft structure or equipment installed near the magnetometer. These unwanted magnetic fields are superimposed on the output of the magnetometers' measurement of Earth's magnetic field. The effect of this superposition is to bias the magnetometer output.

If the unwanted magnetic fields are time invariant, they are referred to as "hard iron" errors and can be represented by a vector quantity, δB^b . If the strength and direction of these unwanted magnetic fields is known, their effect can be removed to un-bias the magnetometer readings. It should be noted that the unwanted magnetic fields can also be caused by items external to the vehicle, but since the vehicle is usually moving, the effect of such fields will be temporary. Furthermore, external fields are unlikely to be present in the air or on the water when using this application for marine or flight vehicles. Thus, errors due to external fields can usually be safely neglected (Note that some areas, such as iron ore deposits can cause local deviations in the magnetic field of up to 10 degrees). Items inside the vehicle can generate unwanted magnetic fields that are time varying. For example, such an item would be a current carrying wire. If the current through the wire is time varying, the resulting magnetometer bias will also be time varying and difficult to calibrate. Fortunately, such errors can be managed by taking care during installation of the magnetometers.

There are materials that generate magnetic fields in response to externally applied fields. The field generated by these materials, called "soft irons," can vary over a wide range depending on both the magnitude and direction of the applied external magnetic field. If such materials are present, they will generate a magnetic field that will be superimposed on the magnetometer output as they generate their own magnetic field in

response to Earth's magnetic field. Since the orientation of Earth's magnetic field vector relative to the soft iron materials fixed inside the vehicle changes with vehicle attitude, this gives rise to a varying bias on the magnetometer output.

In a simple one-dimensional case, the magnitude of the soft iron response is proportional to the external magnetic field. The constant of proportionality is a property of the soft iron material and it is referred to as the material's magnetic susceptibility. In this work it will be assumed that this simple linear relationship is sufficient. However, in some cases there can be appreciable hysteresis. In most soft iron materials the hysteresis is small enough that the linear model is sufficient. In a hysteresis-free, three-dimensional case, a 3×3 matrix is required as opposed to a constant of proportionality. This is the C_{si} matrix in Equation 4.51. In most vehicle installations, magnetometers are installed in parts of the vehicle where errors due to soft iron will be small, and thus C_{si} is assumed to be the identity matrix.

Ideally, the three magnetometers that make up the triad are identical. In reality, however, this may not be the case; each magnetometer will have different sensitivities. That is, when all three magnetometers are subjected to an identical magnetic field, the observed output from each will not be the same due to scale factor errors. Calibrating the scale factor error involves determining the multiplicative factor that must be applied to each magnetometer such that the outputs will be the same when subjected to identical magnetic fields. In the three-dimensional case, the multiplicative constant is the 3×3 diagonal matrix, C_{sf} .

The last remaining error source in the Equation 4.51 is the misalignment error matrix, C_m . In an ideal installation, the magnetometer triad will be mounted in perfect alignment with the body axis of the vehicle. If reasonable alignment is not achieved, however, errors in the magnetometers' outputs will be present due to cross coupling of the

magnetic field axes. If care is taken during the installation process, the misalignment between the triad and the vehicle body axes can be minimized (Note that in a real world case, it would be far easier to estimate the misalignment error rather than try to achieve perfect mechanical mounting). Rotating the body full circle while on a level platform can extract the pitch and roll misalignments, but not the yaw. For the analysis that follows it is assumed that the magnetometer misalignment has been removed and hence the term C_m is the identity matrix. In most vehicle applications, the two largest error sources addressed in magnetometer calibration algorithms are hard iron biases and scale factor errors.

SECTION 4.7.3 MAGNETOMETER SWINGING

Two-magnetometer heading determination systems have been used extensively in navigation applications. Traditionally the sensors used in these systems were flux-gate or flux-valve magnetometers. The method of calibration in the heading domain has been known for over a century [27] and has been used to calibrate modern solid-state magnetometers. This method of calibration is based on perturbation of the basic heading equation (Equation 4.50) and a substitution of the error equations (Equation 4.51). This results in the following heading error equation:

$$\delta\psi = A + B \sin\psi + C \cos\psi + D \sin 2\psi + E \cos 2\psi \quad (\text{EQ 4.52})$$

This is, in effect, a truncated Fourier series where the Fourier coefficients are functions of the hard and soft iron errors. Estimation of the Fourier coefficients is accomplished by a procedure called “swinging.” The procedure involves leveling and rotating the vehicle containing the magnetometer through a series of N *known* headings as shown schematically in Figure 4-12. At each known k^{th} heading, the heading error, $\delta\psi_k$, is computed. These values will be used to form the system of equations (Equation 4.53). The

Moore-Penrose pseudo-inverse, or batch least squares solution of Equation 4.53 yields estimates for the coefficients A through E .

$$\begin{bmatrix} \delta\psi_1 \\ \delta\psi_2 \\ \dots \\ \delta\psi_N \end{bmatrix} = \begin{bmatrix} 1 & \sin\psi_1 & \cos\psi_1 & \sin 2\psi_1 & \cos 2\psi_1 \\ 1 & \sin\psi_2 & \cos\psi_2 & \sin 2\psi_2 & \cos 2\psi_2 \\ \dots & \dots & \dots & \dots & \dots \\ 1 & \sin\psi_N & \cos\psi_N & \sin 2\psi_N & \cos 2\psi_N \end{bmatrix} \begin{bmatrix} A \\ B \\ C \\ D \\ E \end{bmatrix} \quad (\text{EQ 4.53})$$

There are three major drawbacks with this calibration method which necessitated the development of the new calibration algorithm. A shortcoming of the method which becomes apparent when examining Equation 4.50 is that heading is a required input. Since heading errors due to hard and soft iron errors are not constant but heading dependent, the heading input into the algorithm will be corrupted by a non-constant bias. Thus, the first drawback is that another independent measurement of heading is required when calibrating magnetometers using this method.

When performing this calibration for a magnetometer triad installed in an aircraft, the standard practice is to use a compass rose painted on the tarmac as shown in Figure 4-12, as the secondary independent heading measurement. The second drawback is that some of the coefficients, A through E , are functions of the Earth's local magnetic field strength. That is, if the vehicle with the magnetometers is expected to travel over a large geographic area, there will be large variations in the Earth's local magnetic field vector and multiple calibrations must be performed (in practice the errors are simply tolerated). Each calibration will yield a location dependent coefficient set A through E that can be scheduled as needed. Lastly, this method can only calibrate heading in the two dimensional case. If the magnetometers are not going to be used in a heading determination system or if the system consists of three orthogonal magnetometers, then this calibration algorithm is not applicable.

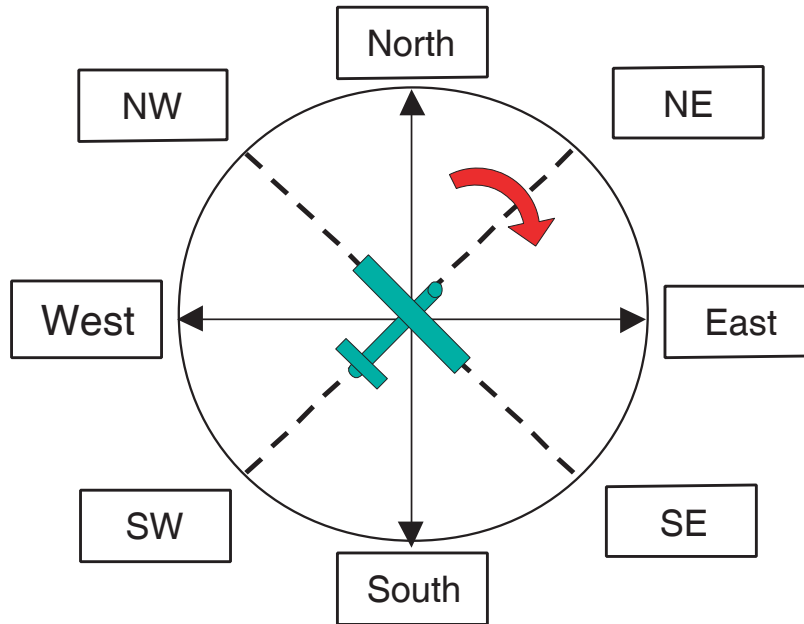


Figure 4-12 Graphical depiction of magnetometer calibration via “swinging.” The aircraft is set upon a known heading reference (usually a painted compass rose at an airport) and “swung” through different known headings. Based on the readings of the magnetometers at each heading, a set of Fourier coefficients can be computed to solve for the biases in heading.

SECTION 4.7.4 ALGORITHM DEVELOPMENT

Unlike the swinging algorithm, a new calibration method has been developed that requires no external reference, nor is it location dependent. The algorithm will be detailed first in the two dimensional case, and then extended to three dimensions. The calibration method is based on the observation that the locus of error-free measurements from two perpendicularly mounted magnetometers is a circle. This can be shown as follows:

$$(B_x^b)^2 + (B_y^b)^2 = B_H^2 \cos^2 \psi + B_H^2 \sin^2 \psi = B_H^2 \quad (\text{EQ 4.54})$$

where B_H is the magnitude of the horizontal component of Earth’s magnetic field vector. Equation 4.54 is the equation of a circle with its origin at the center and radius equal to the magnitude of the horizontal component of Earth’s magnetic field. The magnitude of the radius varies with latitude, longitude and altitude because Earth’s magnetic field vector

varies with geographic location. This variation of Earth's magnetic field vector is well known and well modeled. The magnitude of the Earth's local magnetic field vector is determined using the 1999 International Geomagnetic Reference Field model [17].

The effect of the various magnetometer errors described in Equation 4.51 is to alter the shape of the circle described in Equation 4.54. Hard iron biases, for example, shift the origin of the circle. This can be shown mathematically if we consider the case where the x and y components of Earth's magnetic field vector are offset by hard iron biases, δB_{x_0} and δB_{y_0} , respectively. In this case, the measured field strengths, \hat{B}_x^b and \hat{B}_y^b , are given by:

$$\begin{aligned}\hat{B}_x^b &= B_x^b + \delta B_{x_0} \\ \hat{B}_y^b &= B_y^b + \delta B_{y_0}\end{aligned}\tag{EQ 4.55}$$

By substituting the terms of Equation 4.55 into Equation 4.54, it follows that:

$$(\hat{B}_x^b - \delta B_{x_0})^2 + (\hat{B}_y^b - \delta B_{y_0})^2 = B_H^2\tag{EQ 4.56}$$

which is still the equation for a circle of radius B_H , but is now centered on the point $(\delta B_{x_0}, \delta B_{y_0})$. Scale factor errors cause the body x- and y-magnetometer measurements to be different when both are subjected to a magnetic field of the same strength. This can be expressed mathematically as follows:

$$\begin{aligned}\hat{B}_x^b &= (1 + sf_x)B_H \cos \psi \\ \hat{B}_y^b &= -(1 + sf_y)B_H \sin \psi\end{aligned}\tag{EQ 4.57}$$

which can be rearranged as:

$$\left(\frac{\hat{B}_x^b}{1 + sf_x} \right)^2 + \left(\frac{\hat{B}_y^b}{1 + sf_y} \right)^2 = B_H^2\tag{EQ 4.58}$$

which is simply the equation of an ellipse, centered on the origin, with semi-major and semi-minor axes determined by the parameters sf_x and sf_y . When the output of the magne-

tometer is corrupted both by scale factor errors and by hard iron biases, the resulting locus is an ellipse with its center at the point $(\delta B_{x_0}, \delta B_{y_0})$, and the full equation is:

$$\left(\frac{\hat{B}_x^b - \delta B_{x_0}}{1 + sf_x} \right)^2 + \left(\frac{\hat{B}_y^b - \delta B_{y_0}}{1 + sf_y} \right)^2 = B_H^2 \quad (\text{EQ 4.59})$$

In this analysis, the misalignment error is considered to be the identity matrix. However, if misalignment were present, it would have the effect of rotating the semi-major and semi-minor axes with respect to the cartesian x- and y-coordinate system.

The calibration algorithm developed is a parameter estimation problem. When an aircraft with a pair of magnetometers is rotated through 360 degrees about its yaw axis, the locus of body fixed measurements will be an ellipse. The algorithm attempts to fit the best ellipse (in the least squares sense) to the measured data. If misalignment and soft iron errors are minimized during installation, then the parameter estimation unknowns are the hard iron errors and scale factor errors. In terms of the mathematics of the estimation process, the hard iron errors correspond to the center of the ellipse and the scale factor errors correspond to the size of the major and minor axes of the ellipse. Furthermore, extension of this algorithm to the case of three magnetometers is straight forward: instead of the parameters of an ellipse, the parameters of an ellipsoid are estimated.

There are two ways to carry out the parameter estimation. The first method is to use a classical approach to estimating parameters in a non-linear system of equations such as a non-linear least squares solution (such as the Extended Kalman Filter (EKF) described in [57] and [133]). Specifically, this estimator is based on linearizing the locus described in Equation 4.59. The governing non-linear equations are linearized such that the perturbations of the parameter of interest are estimated. The estimated perturbations are added to non-perturbed variables and the estimation is repeated until convergence is

achieved. It is an iterative procedure and requires a good initial guess of the scale factors and hard iron biases to begin the algorithm.

The EKF approach was simulated extensively in [44] and found to be sensitive to primarily three effects: a good initial guess of scale factor and biases was required for convergence, large sampling noise caused the EKF to diverge, and a large portion of the ellipsoid surface was required for convergence.

The second method for parameter estimation uses a non-linear, two-step estimator. The non-linear two-step estimator, which solves the parameter identification problem by breaking the estimation process into two steps, is an adaptation of the estimator introduced in [62]. In the first step, a set of variables (called first step states) are defined as a combination of the various parameters to be estimated. The estimation problem is linear in these first step state variables and therefore retains the desirable properties of linear systems. Following estimation of the first step states, the second step states, which are the scale factors and hard iron biases, are extracted from the first state steps through algebraic manipulation. The art in this process consists of properly identifying the first step states.

Derivation of the equations for the non-linear, two-step estimator begins by expanding the locus equation Equation 4.59. By multiplying up from the denominator and rearranging, the equation can be rewritten in matrix form as:

$$\begin{bmatrix} (\hat{B}_x^b)^2 \end{bmatrix} = \begin{bmatrix} 2\hat{B}_x^b - (\hat{B}_y^b)^2 & 2\hat{B}_y^b & 1 \end{bmatrix} \begin{bmatrix} \delta B_{x_0} \\ k_2 \\ k_2 \delta B_{y_0} \\ k_1 - (\delta B_{x_0})^2 - k_2 (\delta B_{y_0})^2 \end{bmatrix} \quad (\text{EQ 4.60})$$

where:

$$k_1 = (1 + sf_x)^2 B_H^2 \quad (\text{EQ 4.61})$$

$$k_2 = \frac{(1 + sf_x)^2}{(1 + sf_y)^2} \quad (\text{EQ 4.62})$$

Equation 4.60 represents a single point. If multiple measurements are taken and the left hand side of the equation is stacked with all of the measurements, as is the first matrix on the right hand side of the equation, then the parameters of the vector can be obtained in a least squares sense using the pseudo-inverse. Once the parameter vector is known, then algebraic manipulation will extract the relevant scale factors and biases using Equation 4.61 and Equation 4.62. In order to gauge the effectiveness of this algorithm, a simulation study was carried out.

The simulation is shown in Figure 4-13. The original centered circle is shown in red. Scale factors then distort the circle into an ellipse (blue), and biases finally move the center of the ellipse (green). The green dots represent noisy sampled data of the final ellipse. Using this sampled data, the algorithm is run to determine the scale factors and biases. The only additional information that is available to the algorithm (other than the green points themselves) is the known radius of the red circle. Using the estimated scale factors and biases, the green points are transformed to remove the bias and scale factor effects. The result of that transformation is the red dots scattered along the original circle. Note that the entire ellipse was not required (the amount of the circle required depends on the level of noise, more noise required more information i.e. more of the circle). Again, the only additional information required was the radius of the original circle.

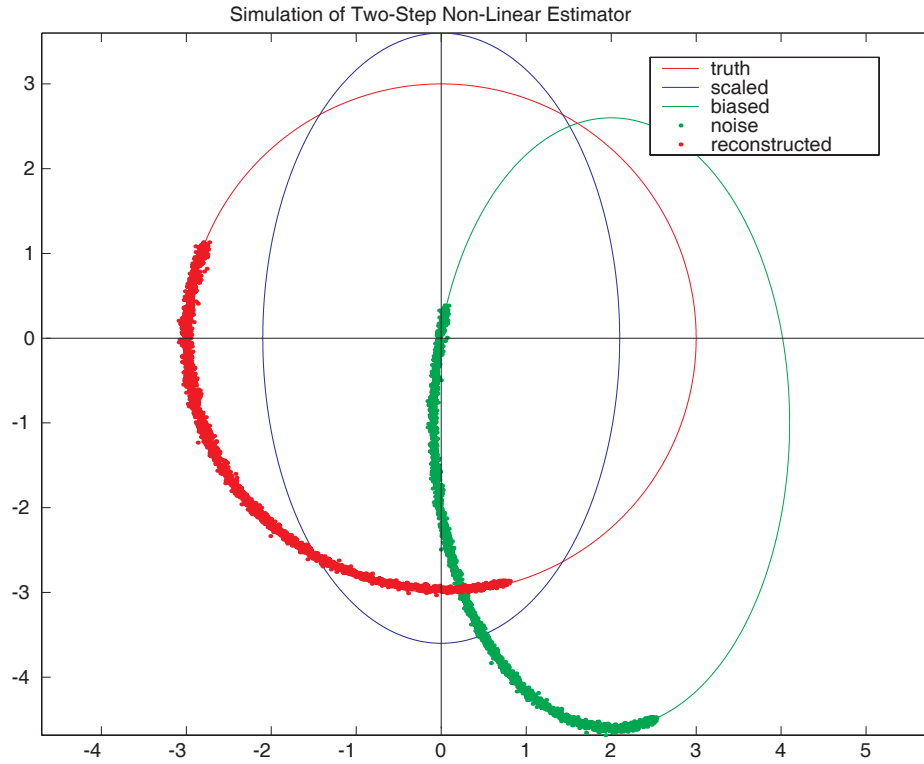


Figure 4-13 Simulation of the two-step calibration algorithm for a 2-D case. The red solid line represents the true response of the magnetometer. It is then distorted by scale factors, stretching the red circle into the blue ellipse. Then it is corrupted by biases, shifting the blue ellipse to the off centered green ellipse. Noisy data from that ellipse (green dots) are run through the calibration algorithm, resulting in a calibration that remaps those points into the red dots, on the original response circle.

The three dimensional case is a simple extension of the two dimensional case. The governing ellipse equation becomes an equation for an ellipsoid:

$$\left(\frac{\hat{B}_x^b - \delta B_{x_0}}{1 + sf_x} \right)^2 + \left(\frac{\hat{B}_y^b - \delta B_{y_0}}{1 + sf_y} \right)^2 + \left(\frac{\hat{B}_z^b - \delta B_{z_0}}{1 + sf_z} \right)^2 = \|B\|^2 = R^2 \quad (\text{EQ 4.63})$$

and this can be rearranged into the following matrix form:

$$\begin{bmatrix} -(\hat{B}_x^b)^2 \\ -(\hat{B}_y^b)^2 \\ -(\hat{B}_z^b)^2 \end{bmatrix} = \begin{bmatrix} -2\hat{B}_x^b & (\hat{B}_y^b)^2 & -2\hat{B}_y^b & (\hat{B}_z^b)^2 & -2\hat{B}_z^b & 1 \end{bmatrix} \begin{bmatrix} \delta B_{x_0} \\ k_2 \\ k_2 \delta B_{y_0} \\ k_3 \\ k_3 \delta B_{z_0} \\ k_4 \end{bmatrix} \quad (\text{EQ 4.64})$$

where:

$$k_1 = (1 + sf_x)^2 R^2 \quad (\text{EQ 4.65})$$

$$k_2 = \frac{(1 + sf_x)^2}{(1 + sf_y)^2} \quad (\text{EQ 4.66})$$

$$k_3 = \frac{(1 + sf_x)^2}{(1 + sf_z)^2} \quad (\text{EQ 4.67})$$

$$k_4 = -k_1 + (\delta B_{x_0})^2 + k_2(\delta B_{y_0})^2 + k_3(\delta B_{z_0})^2 \quad (\text{EQ 4.68})$$

In this case, samples of the points along the surface of the ellipsoid are stacked, and the pseudo-inverse is used to extract the right most column of Equation 4.64. Then algebraic manipulations using Equation 4.65, Equation 4.66, Equation 4.67, and Equation 4.68 are performed to yield the biases and scale factors which most perfectly transform the sampled data into a sphere of radius, R , centered on the origin.

SECTION 4.7.5 EXPERIMENTAL SETUP

Figure 4-14 shows the experimental setup used to validate the calibration algorithm on the three-axis strap-down magnetometers. The yellow box on the end of the wooden boom contains a Honeywell HMR-2003 three-axis strap-down magnetometer hybrid. It is placed on the wooden boom to remove it from the magnetic fields generated by the power supply for the inertial navigation system (INS) that is located behind the



Figure 4-14 Experimental setup to validate magnetometer calibration algorithm. The yellow box at the end of the wooden boom contains the Honeywell HMR-2003 three-axis magnetometers and a microcontroller. It was placed out at the end of the wooden boom to minimize the effect of the magnetic fields of the INS power supply located beneath the orange box. Data was taken by pitching, rolling, and yawing the entire setup repeatedly.

screen, below the orange case. The INS below the orange box is a Honeywell YG-1851 navigation grade INS with rate gyroscopes whose drift rates are less than 0.01 degree/hour. The INS provides a truth measurement. Because the drift rates on the INS gyroscopes are so low, it is able to detect Earth's rotation rate, and lock onto its own attitude. Once this process is complete, the INS will continue to track attitude with a very high degree of accuracy (Note that this kind of accuracy is available only on very, very expensive sensors).

In order to generate points of the surface of the ellipsoid, the entire setup pictured above was rolled, pitched, and yawed in order to measure the various components of Earth's magnetic field. Note that the easiest motion to achieve was yaw and thus most of the point traces are loops around the surface of the ellipsoid. This is due to the fact that Earth's magnetic field has a dip of approximately 70 degrees in the San Francisco area (i.e., the magnetic field vector points into the ground at approximately 70 degrees). Thus a

simple yaw motion with the magnetometers perfectly level will trace out a circle on the top of the ellipsoid. As the magnetometer is pitched up and then yawed again, a new circle will be traced which will translate down the surface of the ellipsoid toward the positive y-axis. Rolls will move the circle toward the negative x-axis.

SECTION 4.7.6 EXPERIMENTAL RESULTS

The setup pictured in Figure 4-14 was tilted up and down, side to side, and yawed

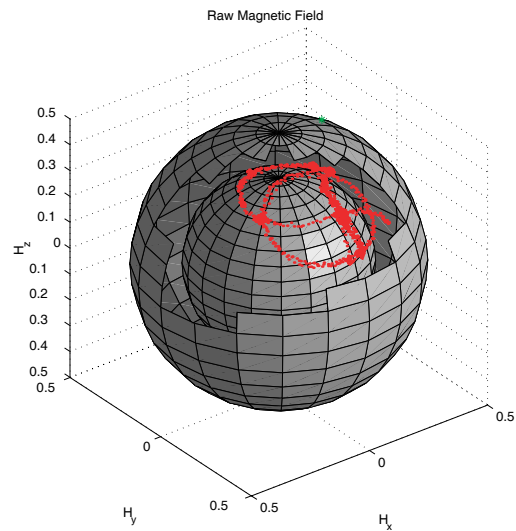


Figure 4-15 Plot of the measured components of Earth's magnetic field before calibration, along with a sphere of radius equal to the magnitude of Earth's magnetic field. This is the raw data recorded from the magnetometers on the wooden boom in the previous figure. In order to see the actual trace, portions of the sphere had to be removed, as the scale factors are less than one. In addition, close inspection will reveal that the trace lies to the right and behind the smaller sphere, indicating the presence of bias errors as well.

about several times in each direction over the course of an hour. The body-fixed magnetic field was recorded along with true attitude from the INS. The three components of the uncorrected magnetic field are plotted and a reference sphere of radius $\|\vec{B}\|$ is plotted in Figure 4-15. Because the scale factors are less than one, the trace can not be seen. Thus, portions of the outer reference sphere are removed in order to see the actual trace and a

smaller reference sphere inserted into the plot. Note that in addition to the scale factors, careful inspection shows the trace to lie above and off to the right side of the smaller, inner reference sphere. This indicates biases on the z- and y-axes.

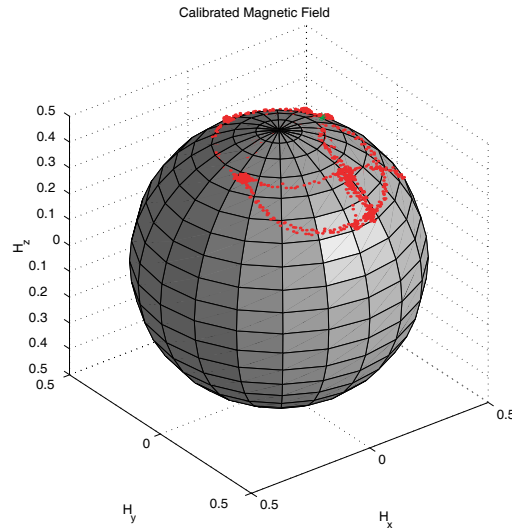


Figure 4-16 Plot of the measured components of Earth's magnetic field after calibration, along with a sphere of radius equal to the magnitude of Earth's magnetic field. Note the excellent agreement between the data and the surface of the sphere. This indicated that the algorithms has matched the biases and scale factors very well indeed.

Figure 4-16 shows the same data plotted after calibration. Note that the trace is now very well aligned with the surface of the reference sphere and that it does not penetrate the surface. This shows that the algorithm performs phenomenally well using even crude, noisy data. In order to better view the agreement of the calibrated data to the surface of the sphere, Figure 4-17 shows the magnitude of the measured magnetic field before (in blue) and after calibration (in red) through time. What can be seen here is the very poor agreement with a constant magnitude magnetic field before calibration and an excellent agreement afterwards. Indeed, the post calibration residuals are on the order of 0.005 gauss, or 1% of Earth's total magnetic field. This is well within the magnetometer specifications. Histograms of the residuals show them to be wide-band noise that could be low-pass filtered for a smoother solution. The residuals are slightly larger towards the end

of the experiment. This is due to dynamics; at this point the wooden boom was highly loaded and most likely flexing.

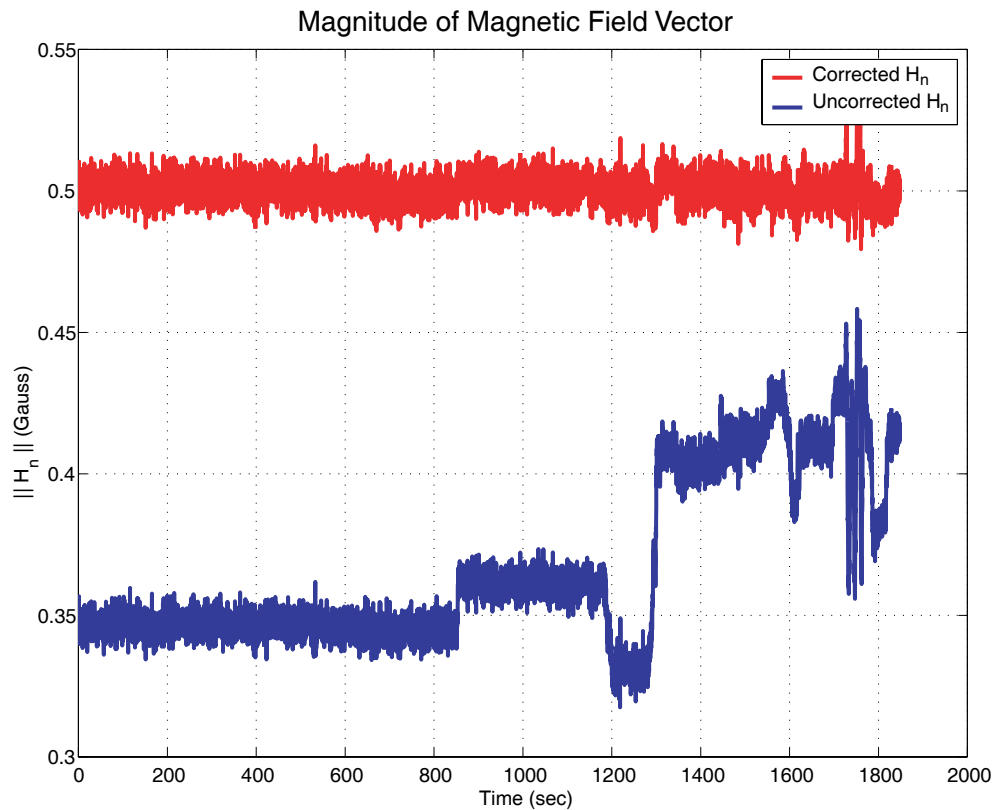


Figure 4-17 Magnitude of body-fixed magnetic field measurements before and after calibration. The initial period was used to generate static statistics on the sensors, and starting at approximately 800 seconds, the large motion was begun. Note that the pre-calibration data (shown in blue) was not even remotely constant, but that the post calibration data (shown in red) gives an excellent measure of the strength of the magnetic field.

The final check of the algorithm was performed in the heading domain. The heading error residual was computed by taking the difference between the heading generated by the magnetometer triad (post calibration) and the heading information from the INS. The errors were found to have a standard deviation of approximately 3 degrees and were again distributed as wide-band noise which could be filtered if this heading information were to be used for vehicle guidance.

Note that while this new calibration algorithm was developed and tested on a strap-down three-axis magnetometer, it is completely general. It could be used to calibrate any three-axis strap-down sensor as long as the magnitude of the total measurement remained constant and was known.

SECTION 4.8 EXPERIMENTAL VALIDATION

With the magnetometer calibrated and attitude estimation algorithms ready, a flight test was set up to validate the algorithms using real sensors and actual flight parameters. The flight test vehicle is a Beechcraft/Raytheon QueenAir, twin engine propeller driven aircraft. This aircraft has been heavily instrumented and has been used extensively in WAAS and LAAS experimentation at Stanford University. It is pictured below, in Figure 4-18.

SECTION 4.8.1 FLIGHT TEST SETUP

A block diagram of the experimental setup used to validate this algorithm is shown in Figure 4-19. Experimental validation of the two vector matching algorithm was performed on a Beechcraft/Raytheon QueenAir test aircraft (Figure 4-18). This aircraft is equipped with several high quality sensors. For attitude reference a Honeywell YG1851 IRU navigation-grade (1 nm/hr. drift) inertial navigation sensor (INS) unit was used to record position and attitude at 50 Hz. The data from the INS was recorded on a separate computer and later aligned with the GPS-time-tagged data. A second, less expensive inertial measurement unit (CrossBow DMU-FOG) was used to send data to the main computer at a rate of 125 Hz. These measurements are also aligned to GPS time internally.



Figure 4-18 Beechcraft/Raytheon QueenAir used for experimental testing of attitude algorithm. This aircraft is equipped with a short baseline GPS attitude system, a Honeywell HMC-2300 digital three-axis magnetometer, Crossbow DME-FOG, and a navigation grade INS. The aircraft was instrumented using the gyroscope-free quaternion attitude estimator and flown through various steep turns. The attitude was found to be in excellent agreement with the INS.

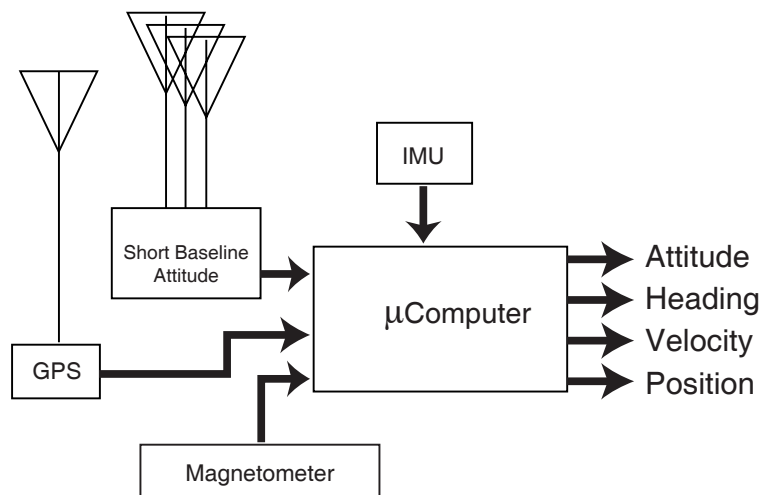


Figure 4-19 Simple block diagram of hardware used for experimental validation of attitude system. The aircraft, a Beechcraft/Raytheon QueenAir is equipped with many high quality sensors. A short baseline attitude system developed at Stanford University, along with a Honeywell navigation grade INS provide attitude. In addition, a Crossbow fiber-optic attitude heading reference system and a Honeywell HMC-2300 digital three-axis magnetometer are all synchronously sampled and aligned with GPS time.

The raw output of the Crossbow DMU accelerometers was used as the body-fixed accelerometer measurements, \vec{g}^b . The local level acceleration, \vec{a} , was computed by differencing velocities derived from GPS augmented by WAAS (again, in a numerical differentiation scheme). This measurement was used to correct the aircraft apparent gravity (accelerometer specific force) measurements during turns. A low cost magnetometer triad (Honeywell HMR 2300) was used to measure Earth's magnetic field vector in the body frame, \vec{B}^b . The output of the magnetometer was recorded serially on the main computer and aligned with GPS-time at 1 Hz.

The known portion of the vector measurements, Earth's gravitational field and magnetic field vector in the navigation frame (i.e., \vec{g}^n and \vec{B}^n), are well known and readily modeled. Earth's magnetic field was modeled using Schmidt-normalized coefficients from the 1995 International Geomagnetic Reference Field [17] as a function of GPS-position. The gravitational field of Earth was assumed to remain down in the local level coordinate frame (navigation frame), and to have a magnitude of 9.81 m/s^2 . The accelerometers of the DMU are MEMS accelerometers similar to those used in the final system.

The test flight lasted approximately 45 minutes from takeoff to landing and included many steep turns. Pitch and roll doublets were also performed in order to deviate from straight and level flight. Following the flight, the data was aligned to GPS-time in post-processing, and the magnetometer and accelerometer data were aligned to each other in order to simulate running the system in real time. Data from the Honeywell INS was interpolated to match the sample points of the magnetometer and accelerometers. Finally, the difference of GPS velocity measurements (numerical differentiation) were used to obtain the measurement of \vec{a}^n . This measurement could have been improved by using a simple Kalman smoother, but for this experiment the added complexity was not deemed justified.

The accelerometer bias and scale factor calibration was already performed internally by the Crossbow DMU, thus no further processing of the accelerometer data was required. The magnetometer required calibration for misalignment errors, hard and soft iron errors (bias), and scale factors errors. The method for calibrating the magnetometer was discussed previously in Section 4.7 on page 122.

The Kalman filter implementation, previously described, was used to estimate the attitude using the post-processed data. An initial guess of the quaternion estimate, \hat{q} , and the initial error quaternion, q_e , was used and the Kalman filter run sequentially through the post-processed data. It is important to note that the Kalman filter is providing an estimate of q_e , not \hat{q} . The output of interest is estimated attitude, \hat{q} , and is computed from q_e continuously.

SECTION 4.8.2 FLIGHT TEST RESULTS

Figure 4-20 compares the attitude versus time for the flight. The green line is the attitude computed by the quaternion based solution to Wahba's problem. Note that this estimate is using the Gauss-Markov based Kalman filter with no gyroscopes. Truth is presented as the red dashed line, and is the attitude recorded by the Honeywell INS. In general, agreement with the INS is good, considering the cost of the overall system. On this scale, the estimated and true attitude appear to track each other with virtually no lag whatsoever. Close inspection of the lower of the three panels will reveal rolls in excess of 50 degrees. Several quick roll reversals, as well as pitch doublets were included in the flight to exercise the attitude estimation system. Pitch excursions in excess of +/- 10 degrees are noted in the middle panel. While the agreement between the estimated and true attitude is indeed good, several areas of poor tracking (most notably in pitch) can be seen.

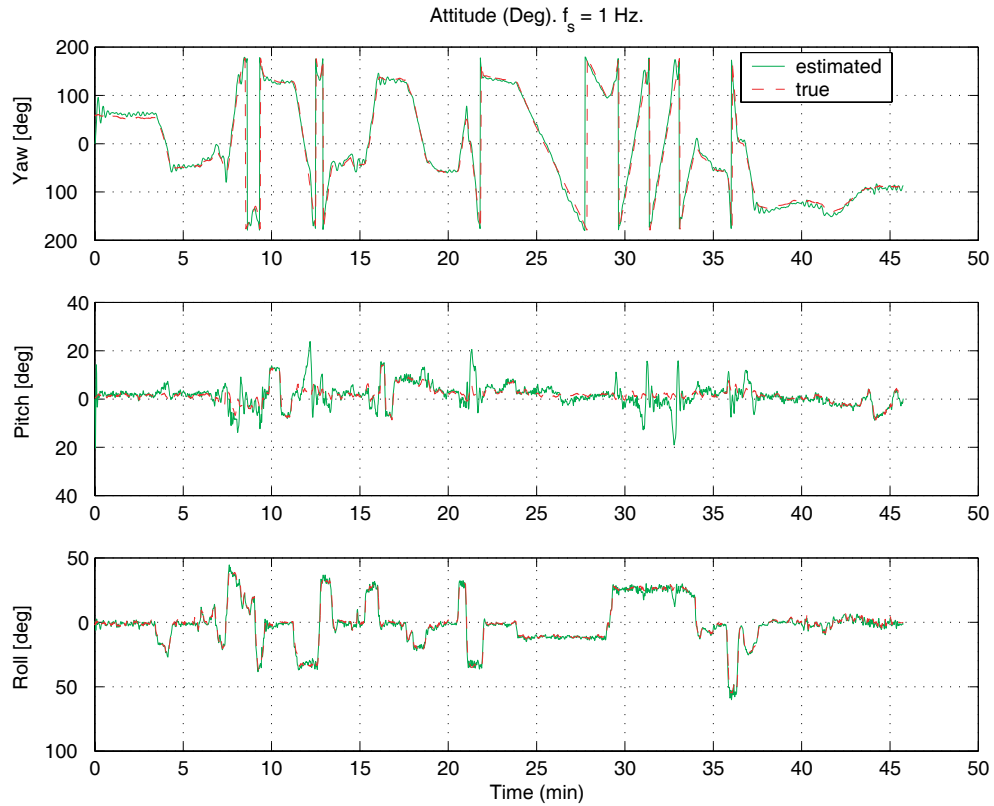


Figure 4-20 Performance of attitude estimation algorithm on actual flight data, presented in Euler angles. The algorithm does an excellent job of matching the INS output (red). A few notable exceptions can be seen, especially in pitch (for example, at 12 minutes into the flight). Note that at this time the yaw is at -90 degrees and decreasing, i.e., the aircraft is turning from west to south, and the local apparent down lines up closely with the magnetic field. This violates the initial assumption of two non-colinear vectors.

For the entire flight, the means and standard deviations for the vector matching Kalman filter (truth provided by INS) are summarized in Table 4-1. There are three main

	μ [deg]	σ [deg]
yaw	0.8313	10.507
pitch	-0.0959	3.6945
roll	-0.7570	2.0624

Table 4-1: Statistics from the gyroscope-free quaternion attitude estimation algorithm on flight test data given for Euler angles (degrees). Much of the large standard deviations is due to the excursions explained in the previous figure. Even with this deviation from the basic premise of the algorithm, the performance is excellent.

causes for the relatively large errors. The first is poor placement of the magnetometer inside the fuselage of the aircraft. The logical place to place the magnetometers are at the wing tip or on top of the rudder as far away from the electronics as possible. The second source of errors is due to a difference in time base between the recorded measurements of the INS and the attitude system. Without synchronous measurements, residual errors from interpolation remain present. The third reason is vector alignment as explained below.

Several times in the flight, the pitch measurement appears to diverge from the INS but then recovers. Close inspection of Figure 4-20 will show that the yaw oscillates from the true attitude at the same time. These divergences appear periodically, at 8, 13, 17, and 22 minutes into the flight, and during the time from 29-33 minutes and 36-37 minutes. The reason that the algorithm performs poorly during these transients is that during a coordinated turn the maneuvering aircraft periodically aligns the body z-axis with the magnetic field of Earth. This condition violates the basic requirement that the two vectors be non-colinear. During this transient moment, while the aircraft nose swings through due east or due west, the magnetic field vector is aligned with the aircraft specific force (apparent gravity), $\vec{a} - \vec{g}$. During this transient, there is insufficient information to determine aircraft attitude. The Kalman filter, however, continues to perform albeit at a degraded performance level even with the lack of gyroscopes. Rate gyroscopes would allow the attitude determination algorithm to bridge these outages without the large transients, but with increased cost and complexity.

It is important to clarify that the large transients are not a failure of the algorithm itself, but rather an operation outside the assumptions of the basic Wahba's problem. The roll angle is such that the local apparent gravity is approximately equal to the magnetic dip and the yaw angle lines up the aircraft apparent gravity vector with Earth's magnetic field. This only happens when the nose of the aircraft is turning through a yaw angle of +/- 90 degrees. Close inspection of the results verifies that this is indeed the case.

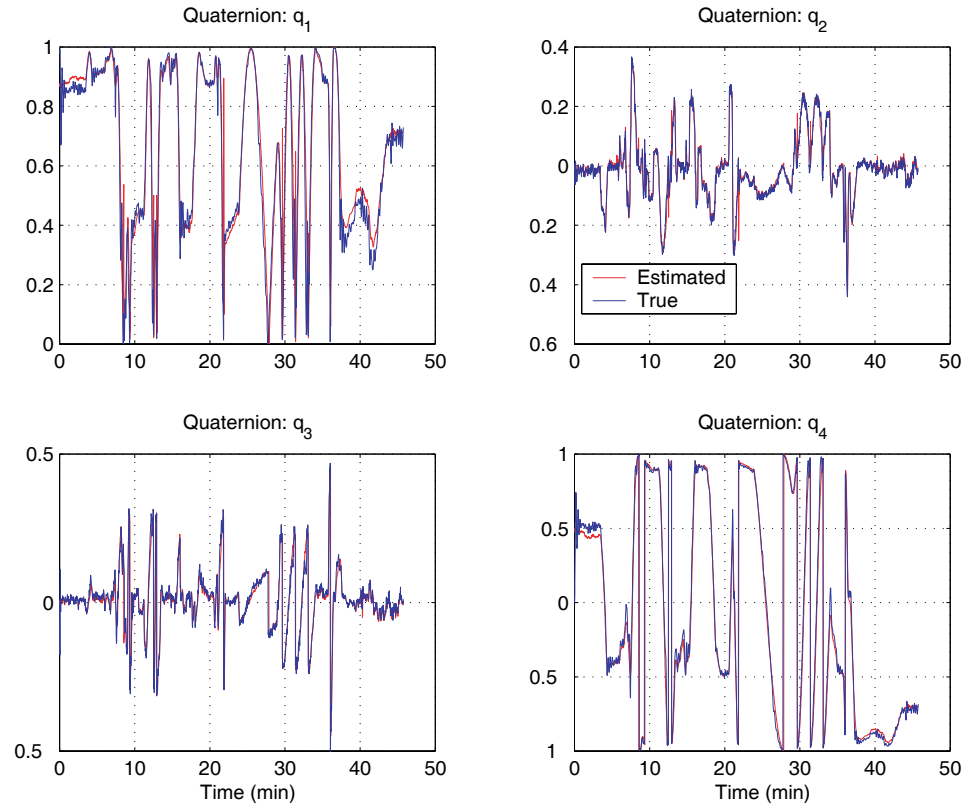


Figure 4-21 Performance of gyroscope-free quaternion attitude estimation algorithm on flight test data, presented as quaternions. Note that in the quaternion domain, the excursions in pitch are much harder to locate. Again, the performance of the algorithm matches the INS quite well, even during some rather “sporty” maneuvering.

Without these transients, where the basic assumptions of the algorithm are not violated, the tracking performance is much better. In order to find a best case scenario for the algorithm, the longest continuous section of maneuvering flight in which this vector aligning did not occur was used to gather statistics. As this turned out to be a four minute section with large turns and moderate pitch excursion, it is felt that the statistics are valid. Thus the section of the flight from 22 to 26 minutes of the flight, which includes a minute long steep banked turn, is used to compute best case scenario statistics for the attitude

algorithm. The tracking performance is much better and is summarized in Table 4-2 below:

	μ [deg]	σ [deg]
yaw	-0.8225	3.286
pitch	0.9517	1.3801
roll	-0.9959	1.2596

Table 4-2: Statistical performance of the gyroscope-free quaternion attitude estimation algorithm over best-case scenario on real data, presented as Euler angles (degrees). These statistics are compiled over a section of flight that included maneuvering, but did not swing the local apparent down in line with the magnetic field. The residual errors are very small, but are likely caused by a temporal misalignment between the magnetometer data and the INS data. Actual performance on the sailboat showed errors that were much smaller.

This should be considered as the best-case performance of the gyroscope-free quaternion-based attitude determination algorithm. Finally, the aircraft environment is very poor for the performance of the magnetometer, given the large electromagnetic transients that cannot be calibrated out of the measurements. Also, the interpolation and alignment of the INS data introduces some errors that are difficult to quantify.

SECTION 4.9 STATIC BOAT TEST

In order to differentiate between the aircraft tests and the expected performance that would be encountered on the sailboat, a series of static tests were performed. In order to perform the experiments, the boat was set upon its trailer at the center of a larger parking structure. Every attempt was made to ensure that the boat was level and oriented to point the nose of the boat towards true north. This was done with a magnetic compass and a large bubble level.

With the boat leveled and pointed north, the boat attitude system was turned on and allowed to collect data for approximately six hours. Unfortunately, no truth system

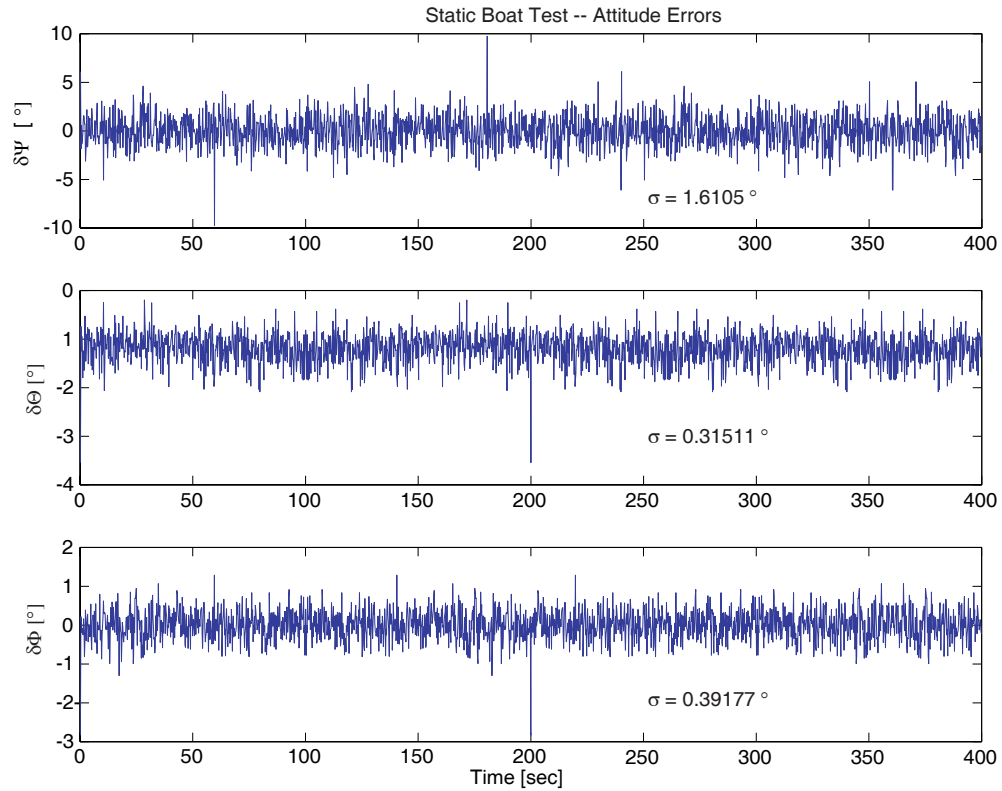


Figure 4-22 Static boat attitude errors. These errors are based on placing the boat trailer in a parking garage and leveling the boat as best as possible. A few minutes of typical data are presented. Because there is no independent source of truth, only the standard deviations of the attitude errors are reported. This shows that the standard deviations are approximately 1.5 degrees in yaw and less than 0.5 degrees in both pitch and roll.

was available, so that the bias in the attitude system could not be directly measured. Note that the biases were small and most likely attributed to poor alignment of the boat with north and level than errors in the sensors, but this cannot be separated. Based on this data, the standard deviations of the attitude system are reported in Table 4-3 below.

	σ [deg]
yaw	1.6105
pitch	0.3151
roll	0.3918

Table 4-3: Standard deviations of the static attitude data taken from the sailboat upon its trailer in the parking garage. Note that due to the lack of an independent measurement of truth, the mean of the error is not reported. Rather, only the standard deviation is presented for yaw, pitch, and roll.

SECTION 4.10 CONCLUSIONS

An attitude determination system was built for the Atlantis that is based on two vector measurements of non-zero, non-colinear vectors. The algorithm is based on a quaternion formulation of Wahba's problem, whereby the error quaternion (q_e) becomes the observed state and can be cast into a standard linear measurement equation. Using Earth's magnetic field and gravity as the two measured quantities, a low-cost attitude determination system was developed into a real-time attitude system. An iterated least squares solution to the attitude determination problem was simulated on static cases and shown to be globally convergent. A time-varying Kalman filter implementation of the same formulation is tested on simulated dynamic data, as well as on experimental data from a maneuvering aircraft.

In addition, a non-linear two-step estimation algorithm for calibrating solid-state strap-down three-axis magnetometers was developed. This calibration algorithm is general, and allows estimation of any three-axis vector measurement errors. If the sensor is perfectly aligned with the body axes (or the misalignment matrix has been separately estimated), then the procedure for estimating the errors does not require any external reference, only the magnitude of the vector that is being measured. In the specific case presented in this thesis, the estimated errors are used to calibrate the magnetometer for the attitude system. This calibration technique is both robust and accurate; the robustness was demonstrated experimentally by converging even in the presence of considerable sensor noise. Further, the algorithm required only a small portion of the ellipsoid locus for the estimation process to work.

The best case performance of the system in the aircraft was roughly 3 degrees in yaw and 1 ½ degrees for pitch and roll. Rate gyroscopes would improve the response, allowing the true dynamics to be tracked through the outages, but with the penalty of more

expensive hardware. Static tests on the catamaran showed much better performance, with errors of $1\frac{1}{2}$ degrees in yaw, and less than $\frac{1}{2}$ degree in pitch and roll, with no tendency to drift whatsoever. This low cost system was able to reliably provide a full attitude solution at a 10 Hz rate (limited by the GPS velocity output rate) at a fraction of the cost of gyroscope-based systems.